 doi:10.20944/preprints202012.0770.v2

Article

Targeting BRF2 in Cancer Using Repurposed Drugs

Behnam Rashidieh [1,*], Maryam Molakarimi [2], Ammar Mohseni [2], Simon Manuel Tria [1,3], Hein Truong [1], Sriganesh Srihari [1], Rachael C. Adams [1], Mathew Jones [4], Pascal H.G. Duijf [5,6,7], Murugan Kalimutho [1] and Kum Kum Khanna[1,*]

1 QIMR Berghofer Medical Research Institute, 300 Herston Road, Herston, QLD 4006, Australia
2 Department of Biochemistry, Faculty of Biological Sciences, Tarbiat Modares University (TMU), Nasr Bridge, Tehran 14115-154, Iran
3 School of Environment and Science, Griffith University, Nathan, QLD 4111
4 The University of Queensland Diamantina Institute, Faculty of Medicine, The University of Queensland, Brisbane, QLD 4102, Australia
5 Institute of Health and Biomedical Innovation, Queensland University of Technology (QUT), Faculty of Health, School of Biomedical Sciences, Brisbane QLD, Australia
6 Centre for Data Science, Queensland University of Technology (QUT), Brisbane QLD, Australia
7 University of Queensland Diamantina Institute, The University of Queensland, Translational Research Institute, Brisbane QLD, Australia
* Correspondence: Kumkum.Khanna@qimr.edu.au (K.K.K.); Behnam.Rashidieh@qimrberghofer.edu.au (B.R.)

Simple Summary: BRF2, a subunit of RNA polymerase III transcription complex, is upregulated in a wide variety of cancers and is a potential therapeutic target; however, no effective drugs are available to target BRF2. Upregulation of *BRF2* in cancer cells confers survival by prevention of oxidative stress-induced apoptosis. In this manuscript, we report the identification of potential BRF2 inhibitors through *in silico* drug repurposing screening. We further characterized Bexarotene as a hit compound for the development of BRF2 selective inhibitor and provide experimental validation to support the repurposing of this FDA-approved drug as an agent to reduce cellular levels of ROS and consequent BRF2 expression in cancers with elevated levels of oxidative stress.

Abstract: Overexpression of BRF2, a selective subunit of RNA polymerase III, has been shown to be crucial in the development of several types of cancers, including breast cancer and lung squamous cell carcinoma . Predominately, BRF2 acts as a central redox-sensing transcription factor (TF) and is involved in rescuing oxidative stress (OS) -induced apoptosis. Here, we showed a novel link between BRF2 and DNA damage response. Due to the lack of BRF2 specific inhibitors, through virtual and molecular dynamics screening, we identified potential drug candidates that interfere with BRF2-TATA-binding Protein (TBP)-DNA complex interactions based on binding energy, intermolecular, and torsional energy parameters. We experimentally tested Bexarotene as a potential BRF2 inhibitor. We found that Bexarotene (Bex) treatment resulted in a dramatic decline in oxidative stress (Tert-butylhydroquinone (tBHQ))-induced levels of BRF2 and consequently, lead to a decrease in cellular proliferation of cancer cells which may in part be due to drug pretreatment induced reduction of ROS generated by the oxidizing agent. Our data thus, provide the first experimental evidence that BRF2 is a novel player in DNA damage response pathway and Bexarotene can be used as a potential inhibitor to treat cancers with the specific elevation of oxidative stress.

Keywords: BRF2; cancer; molecular dynamics simulation; drug repurposing; Bexarotene

1. Introduction

RNA polymerase III (Pol III) is critically important for transcription initiation. Transcription factor IIB-related factor 2 (BRF2) is a Pol III complex subunit which plays a key role in cellular function as a master regulator of oxidative stress, and its overexpression is linked to tumorigenesis[1]. Studies have shown high basal levels of BRF2 expression in breast and lung cancers[2,3], where it is a potential independent prognostic factor for the recurrence and metastasis of lung cancer. BRF2 was identified as a lineage-specific marker

 doi:10.20944/preprints202012.0770.v2

in lung cancer[4] and was later recognized as an oncogenic driver in breast cancer[5] and esophageal carcinoma[6]. The genetic activation of BRF2 has also been linked to lung squamous cell carcinoma and other cancers[7,8]. BRF2 knockdown can inhibit the migratory and invasive abilities of Non-Small Cell Lung Cancer cells (NSCLC) and induce loss of epithelial-mesenchymal transition[7,9,10]. Additionally, BRF2 has been shown to play a crucial role in breast cancers with heterogeneous *HER2* gene amplification. Within such tumors, only 10 to 15% of the cells show amplification of a *HER2* gene signature[3], whereas the remaining population is HER2-negative. By analyzing multiple TCGA cancer datasets, BRF2 has been shown to be significantly upregulated in a HER2-negative compartment of these tumors to compensate for the lack of HER2 amplification[3]. Multiple cancer models have also shown significant alterations in BRF2 copy number variations, specifically copy number gain and amplification[2]. Targeting specific Pol III components, such as BRF2 and other related molecular subunits, could be advantageous due to its specific role in regulating certain aspects of transcription and/or the oxidative stress response. We and others have shown a context-dependent role of BRF2 as a cis-associated 'alternative driver oncogene' with a significant role in lung and ER-/HER2+ breast cancers, respectively[2,4].

BRF2 recruits Pol III complex to essential gene promoters including 5s rRNA, transfer RNA (tRNA), and U6 small nuclear RNAs (snRNAs), hence influences cell proliferation and growth [11], [12]. All Pol III subunits function together with three Transcription Factors (TFs): TFIIIA, TFIIIB and TFIIIC. While TFIIIA is a single protein that is specifically recruited to Type 1 promoter (5s rRNA), TFIIIB consists of three components: TBP (TATA binding protein), BDP1 and either of the TFIIB-related factors BRF1 (for tRNA) or BRF2 (only in type 3 or U6 promoter). The functions of TFIIIs are to recruit Pol III to the transcription start sites through a series of DNA-protein and protein-protein interactions. In order to target BRF2 effectively, the structure, interactions, functions, and regulatory role of this TF, among other subunits and components of the RNA polymerase III (Pol III) machinery, should be taken into consideration. BRF2 recruits RNA Pol III to type III gene external promoters, including the gene product selenocysteine (SeCys) tRNA, which is involved in the synthesis of selenoproteins, and acts to reduce reactive oxygen species (ROS) to maintain cellular redox homeostasis[1]. The absence or defective expression of selenoproteins induces apoptotic cell death[1]. Moreover, high baseline levels of BRF2 have been observed in cancer cell lines that are subjected to prolonged oxidative stress[1]. Therefore, it is speculated that high levels of BRF2 expression in cancer cell lines supports sufficient expression of selenoproteins, in order to detoxify ROS and preserve redox homeostasis, which is a hallmark of cancer cells.

In the current study, we have identified a novel function for BRF2 in regulation of the DNA damage response. Furthermore, we have done in silico screening to target BRF2-TBP-DNA complex and identified potential cancer drugs as candidates. This was followed by experimental validation of Bexarotene drug to study its effect on BRF2 levels and anti-proliferative effects.

2. Materials and Methods

2.1. TCGA Analyses for Genomic Instability

The correlations between gene expression (from The Cancer genome Atlas (TCGA) RNAseq datasets) and 18 features of genomic instability (GI) are listed below:

(1) NtAI: The number of telomeric allelic imbalances[13]. **(2)** LST: Large Scale Transitions; the number of chromosomal breaks between adjacent regions of at least 10 Mb[14]. **(3)** HRD_LOH: Homologous recombination deficiency score; the number of genomic segments with loss of heterozygosity (LOH)[15]. **(4)** Sum_HRD_score: The sum of NtAI, LST and HRD_LOH homologous recombination deficiency signature scores in (1-3)[16]. **(5)** wGII: Weighted Genomic Instability Index[17]. **(6)** ITH: Intra-tumor heterogeneity, a

 doi:10.20944/preprints202012.0770.v2

measure for how heterogeneous an individual tumor sample is, determined using the ABSOLUTE algorithm[18]. **(7)** Ploidy distribution: The ploidy/DNA content; 2 is the equivalent of 2n, the normal/diploid amount, whereas 4 would occur after whole-genome doubling. The larger the deviation from 2, the more aneuploid the cells are. Ploidy was determined using the ASCAT (allele-specific copy number analysis of tumors) algorithm[19]. **(8)** Ploidy groups: In this panel, the ploidy data shown in panel (7) are binned, with "diploid" referring to tumor samples with 2n DNA content, "aneup_lo" referring to tumor samples that are aneuploid but near diploid/2n (either lower or slightly higher than 2n DNA content), "aneup_high" referring to tumor samples that are aneuploid and with DNA content well above 2n, and "aneup_all" referring to all aneuploid tumor samples (sum of former two bins). **(9)** cal_scna_burden: The number of chromosome arm-level somatic copy number alterations. This is the total number of chromosome arms that are gained or lost, also known as chromosome arm aneuploidies (CAA). This was determined using SNP6 array copy number data[20]. **(10)** wc_aneuploidy: The total number of whole chromosomes that are gained or lost. This was determined using SNP6 array copy number data[21]. **(11)** CIN70: A surrogate gene expression signature for chromosomal instability, based on 70 genes. The higher this score, the more chromosome instability is predicted[22]. **(12)** aneuploidy_score_AS: A score for aneuploidy, the sum of the number of chromosome arms and whole chromosomes gained or lost[23]. **(13)** genome_doublings: The number of whole-genome doublings, determined using the ABSOLUTE algorithm[18]. **(14)** silent_mutations_per_mb: Number of silent mutations per mega-base (MB)[24]. **(15)** nonsilent_mutations_per_mb: Number of non-silent mutations per mega-base (MB)[24]. **(16)** HRD_score_Peng: Homologous Recombination Deficiency score. This is a gene expression signature, based on the expression of 230 genes.The higher the score the more likely that there are HR defects in the tumor[25]. **(17)** no_of_MSI_events: Number of microsatellite instability events per sample[26]. **(18)** chromothripsis: Samples negative or positive for chromothripsis[27].

2.2. TCGA Analyses for Cellular Signaling and Immunoregulation

The Spearman correlation analysis between the gene expression levels (mRNA levels from The Cancer Genome Atlas (TCGA) RNAseq datasets) and the variables listed below:

(A) Scores for twelve pathways were determined by the integration of multi-platform data from several types of 'omics' analyses[28]. **(B)** 1. Angiogenesis score: A 43-gene expression signature for the level of angiogenesis[29].2. Hypoxia score (Winter): A 99-gene expression signature for the level of hypoxia[30]. 3. Hypoxia score (West): A 26-gene expression signature for the level of hypoxia[31]4. Hypoxia score (Sorensen): A 27-gene expression signature for the level of hypoxia[32].5. Hypoxia score (Seigneuric): A gene expression signature for the level of hypoxia[33]. 6. Hypoxia score (Ragnum): A 32-gene expression signature for the level of hypoxia[34].7. Hypoxia score (Hu): A 13-gene expression signature for the level of hypoxia[35]. **(C)** 1. Cancer/testis (CT) antigen load. 2. Indel neoantigen load. 3. SNV neoantigen load. **(D)** 1. Autophagy-related prognostic signature: A prognostic gene expression signature based in the weighted expression of 8 autophagy-related genes[36]. 2. Stemness (mRNA): Level of stemness, based on mRNA data[37]. 3. Stemness (DNA methylation): Level of stemness, based on DNA methylation data[37]. 4. Predicted pCR to T/FAC chemotherapy: A 30-gene pharmacogenomic predictor of pathologic complete response (pCR) to preoperative weekly paclitaxel and fluorouracil-doxorubicin-cyclophosphamide (T/FAC) chemotherapy, determined based on 133 patients with stage I-III breast cancer[38]. 5. Proliferation score: A weighted proliferation gene expression signature[39].

For immunoregulation and immune cell infiltration, the levels of 26 tumor-infiltrated immune cell types, or states, were estimated using the tumor immune estimation resource[40].

 doi:10.20944/preprints202012.0770.v2

2.3. Virtual Screening Procedure

A drug library, containing 8,770 compounds in sdf format, has been extracted from the DrugBank database v. 5.1.5 (https://www.drugbank.ca/)[41]. BRF2 and the structure files of drugs have been converted into *pdbqt* format using AutoDock Tools4 software[42,43]. Peptide drug structures and ligand containing Si atoms due to the absence of force-field parameters have been excluded from the analysis. 8000 molecular dockings have been performed using an Autodock Vina 1.1.2 program[44]. Each drug was run through one docking simulation which generated ten docking poses. A box of size x = 66.98 Å, y = 46.90 Å, z = 44.83 Å has been placed over the full structure of BRF2 structure. The 'exhaustiveness' value (the number of runs) was set in default value = 8.

2.4. Molecular Dynamics Simulations for Protein-Ligand Complexes

The three-dimensional structure of BRF2 was extracted from the RCSB Protein Data Bank (PDB ID 4ROC), which is in complex with TBP and DNA molecules. Two sets of Molecular Dynamics (MD) simulations were performed. In the first MD simulation, we investigated the stable conformation of ligand-free BRF2 structure before binding to TBP and DNA molecules. MD simulations and molecular mechanics (MM) minimization were performed using Gromacs 2019.6 package under an amber ff99SB forcefield. MD simulations were carried out with periodic boundary conditions. Van der Waals forces and the Particle-mesh Ewald method were both treated with a cut-off of 10 Å The frequency to update the neighbor list was 5. The protonation state of Gromacs package was used to calculate the total charge of protein. The protein was solvated with TIP3P water molecules with an 8 Å radius buffer zone around the protein in a truncated octahedron periodic box. The systems were neutralized by adding the corresponding number of counterions (Na^+ and CL^-) using the genion module. MD simulation was performed in 4 steps. Firstly, the whole system was minimized by the steepest descent followed by conjugate gradients algorithms. Next, in the equilibration step, using a force constant of 1000 kJ/mol*nm, heavy atoms were restrained allowing the solvent and ions to evolve by MD in the NVT ensemble (200 ps) and minimization. Equilibrium geometry was required to be at 298 K and 1atm. To achieve this, we increased the system temperature and reassigned the velocities at each step based on Maxwell-Boltzmann distribution equilibrated for 200 ps. We set the temperature coupling to 0.1 ps and pressure coupling to 2 ps. For the thermostat and barostat during the equilibration, we used V-rescale and Parrinello-Rahman algorithms, respectively and all bonds were constrained through the LINCS algorithm. In the production which is the final step, we performed 100 ns MD simulation under an NPT ensemble. Nosé-Hoover thermostat and Parrinello-Rahman barostat were used, removing position restraints to retain stable temperature and pressure in the production step. The temperature was at 310 K with a time step of 2 fs. Constraining the lengths of hydrogen-containing bonds was further improved by addition of the LINCS algorithm.

Then the output of the first MD simulation was used as input for virtual screening. One of the best-ranked complexes from virtual screening was minimized and used for second molecular dynamics simulations. To parametrize ligand molecule, GAFF forcefield which was assigned by the Antechamber program in AMBER tools was used. AM1-BCC charge model was used to calculate the atomic point. The coordinate file, in SYBYL mol2 format, was formerly loaded to Antechamber program in order to set these parameters. After generating AMBER topology and coordinate files, these files were converted to GROMACS topology and coordinate files using acpype conversion script. Other conditions are similar to first MD simulation.

2.5. Binding Free Energy Calculations

The binding free energy calculations were performed as described before[45–47]. During the equilibrium step, we analyzed the binding free energies of the complexes between BRF2 and ligand by taking 400 snapshots from 60 to 100 ns MD simulations, using g_mmpbsa tool of Gromacs [48].

2.6. Umbrella Sampling (US) Simulation

The US simulation were performed as described before [48]. Briefly, we selected the average structure from the last 10 ns of the simulation prepared using Gromacs 2019.6 software. We made the complex of protein–ligand parallel to the y-axis and a box with length of 12 nm was constructed to pull the ligand along the y-axis by a 2.5 nm distance. Following neutralization, minimization and equilibration we performed US simulation using the center-of-mass-pulling method. By using a 600 kJ/(mol*nm) force, the ligand was pulled from the protein pocket over the course of 500 ps at the rate of 0.005 nm per ps. We saved the snapshots at each picosecond and 27 snapshots extracted at intervals of approximately 0.1 nm which they were used as starting configurations for each US simulation, (each of them independently simulated for 100 ps by performing NPT equilibration) following by performing 5 ns MDrun. We calculated the potential mean force (PMF) from this US outputs using the weighted histogram analysis method (WHAM). The force (kcal/mol) needed to pull the ligand from the binding pocket and the corresponding distance pulled are demonstrated on the PMF graphs (y and x axes, respectively). The binding free energy (ΔG) was calculated for this ligand by taking the difference between the plateau region of the PMF curve and the energy minimum of the simulation.

2.7. Principal Component Analysis (PCA) and Free Energy Landscape (FEL)

PCA was performed as described previously[48], to attain a mass-weighted covariance matrix of the protein atom displacement. This parameter is indicative of dominant and collective modes of the protein from the total dynamics of the MD trajectory. A set of eigenvectors and eigenvalues reflecting the molecules' concerted motion were extracted by diagonalizing the covariance matrix. To yield the eigenvalues and eigenvectors by calculating and diagonalizing the covariance matrix, we used g_covar following by using g_anaeig tool for plotting and analyzing eigenvectors as well as RMSF value for PC1 and 2. We used the gmx sham for calculating free energy landscape based on PC1 and PC2 eigenvectors. We performed free energy landscape (FEL) for analyzing the conformational changes based on the PCA results. We can identify stable or transient state of biomolecules based on the free energy values of the conformations. The free energy, ΔG(X), is calculated by Equation (ΔG(X)=−KBTInP(X)[49]), where KB is the Boltzmann constant and T is absolute temperature, X represents the PCs, and P(X) is the probability distribution of the conformation ensemble along the PCs.

2.8. Cell Culture

All cells were cultured based on ATTC instructions. Cultures were passaged every 4 days as per manufacturer's instructions (Stem Cell Technologies). HeLa iCas9 cells[50] were grown at 37°C in Dulbecco's modified eagle medium (DMEM) with 10% tetracycline-free fetal bovine serum, 100 U/mL penicillin, and 100 U/mL streptomycin. All the cell lines were routinely tested for Mycoplasma infection by Scientific Services at QIMR Berghofer Medical Research Institute.

2.9. Gene Transduction and Transfection

For the transient BRF2 silencing (reverse transfection) we used 10-20 nM of small interfering RNAs (Shanghai Gene Pharma, China) and Lipofectamine RNAi MAX (Life Technologies™) for 48 hours. For the generation of stable and constitutive cell lines with knockdown of BRF2, we used the small-hairpin RNAs (Sigma Aldrich®, St Louis, USA). For transduction of lentiviral construct, we used the spinfection method for 1 hour in the presence of Hexadimethrine bromide polybrene; (Sigma Aldrich®, St Louis, USA). For selection of clones 5 μg/mL of Puromycin (Life Technologies™) was used.

Sequence: CCGGCCTCAGGAAGTTAGGGACTTTCTCGAGAAAGTCCCTAACTTCCTGAGGTTTTT

The lentiviral particles: SHCLNV-NM_018310 MISSION®, shRNA Lentiviral Transduction Particles

 doi:10.20944/preprints202012.0770.v2

2.10. CRISPR/Cas9-mediated genome editing

Target sequences for BRF2 were selected from the Toronto KnockOut Library V3 (BRF2 gRNA1 - GCAACTGCAGAACTCGACAA BRF2 gRNA2 CCAGTGGA-TATCCATCAGGG) [51]. Target sequences were ordered as 24-nt oligonucleotides with asymmetric 5′ overhangs, phosphorylated using T4 polynucleotide kinase, annealed and cloned into BsmBI-treated lentiGuide-puro (Addgene 52963) with T4 DNA ligase. For stable expression of gene-specific sgRNAs, lentiGuide-puro plasmids were cotransfected with psPAX2 and pMD2.G into Lenti-X 293T cells (Clontech). Supernatants were filtered after 24 to 48 hr, mixed 1:1 with fresh medium containing polybrene (10 μg/mL), and applied to target cells for 16 to 24 hr. Transductants were selected in puromycin (5 to 20 μg/mL). Gene disruption was induced with doxycycline-regulated Cas9 transgene present in the host cell line[50].

2.11. Western Blot and Immunoblotting

Cells were exposed to genotoxic agents (ionizing radiation and cisplatin) and harvested at indicated timepoints. Protein lysate was made by Urea/SDS buffer lysis buffer (50 mM Tris pH 7.5, 7M urea, 1%SDS, 100mM NaCl) and sonicated for 10-15sec. Protein quantification was determined using Pierce™ BCA assay kit (Thermo Scientific) as per manufacturer's protocol. For western blot, 30 μg of protein was loaded on SDS-PAGE gel and electrophoresed at 120 V. Proteins were transferred on Amersham Hybond C nitrocellulose membrane following by staining in Ponceau S to confirm the transferring.

For immunodetection, the membrane was incubated for 1 h in blocking buffer, followed by overnight incubation (4 °C) with the indicated primary antibodies. After 3 washes with PBS/Tween and 1h incubation with peroxidase-conjugated secondary antibody followed by 3Xtimes washing, the immunodetection was undertaken. The detection of signals was based on the chemiluminescence reaction between peroxidase and luminol/hydrogen peroxidase mixture from Western Lightning® Plus ECL followed by development by ChemiDock Imaging System (BioRad).

Table

Primary antibody	
Polyclonal rabbit anti-COX IV (WB-1:1000)	Millennium Science Pty Ltd
Monoclonal Mouse anti-yH2AX (WB, IF–1:1000)	Meck Millipore, Darmstadt
Polyclonal rabbit anti-BRF2 (WB – 1:1000, IF – 1:400)	Sapphire Bioscience, Australia
Polyclonal rabbit anti-p53-s15 (WB – 1:1000)	Sapphire Bioscience, Australia
Polyclonal rabbit anti-phospho KAP1 (WB-1:1000)	Bethyl laboratories, Inc. USA
Monoclonal Mouse anti-RAD51 (WB–1:1000)	GenTex Inc., USA
Polyclonal Rabbit anti-NRF2 (WB–1:1000)	Cruz Biotechnology, Inc, USA
Monoclonal Mouse anti-NBS1 (WB–1:1000)	Becton Dickinson Biosciences, USA
Polyclonal Rabbit anti-MRE11 (WB–1:1000)	Becton Dickinson Biosciences, USA
Polyclonal Rabbit anti-H3 (WB–1:1000)	Abcam®, USA
Secondary antibody	
Polyclonal anti-rabbit-antibody (IgG) Peroxidase-conjugate (from goat) (WB–1:3000)	Sigma-Aldrich, Steinheim
Polyclonal anti-mouse-antibody (IgG) Peroxidase-conjugate (from goat) (WB–1:3000)	Sigma-Aldrich, Steinheim

2.12. MTS assay

MTS cell viability assay (CellTiter 96® Aqueous, Promega, WI, USA) was performed in a 96-well tissue-culture plate (BD Falcon™) with 1000 cells/well seeded and next day treated with drugs/siRNA for 72 hours. 100μl of complete DMEM media containing 10% MTS reagent was added to each well and incubated for 1 hour and plates were read at

 doi:10.20944/preprints202012.0770.v2

490nm on a Biotek Powerwave™ XS2 microplate spectrophotometer (Winosski, VT, USA). Optical density (O.D.) was measured, recorded and normalised to respective control.

2.13 Proliferation assay

Cells were plated in a 24 well plate with four replicates each, seeded at a density of 10,000 cells/well. The cells were allowed to incubate and image in the IncuCyte® S3 Live-Cell Analysis system (Essen BioSciences Inc., USA) for seven days at 3-4 hours interval. The data was analyzed using the complementary Essen IncuCyte® S3 Live-Cell Analysis software. Finally, the graphs were generated using the analyzed data through GraphPad Prism 7.

2.14 Reactive Oxygen Species (ROS) Activity Assay

Cellular ROS Assay Kit (ab113851) with DCF-DA probe was used according to the manufacturer's instructions to determine the ROS activity. The cell-permeant reagent 2',7' –dichlorofluorescin diacetate (DCFDA, also known as DCFH, DCFH-DA, and H2DCFDA) quantitatively assesses ROS (hydroxyl, peroxyl and other radicals) in live cell samples. DCF is highly fluorescent and is detected by fluorescence spectroscopy with excitation/emission at 485 nm / 535 nm. For plate reader measurement, 3,000 cells were seeded in triplicate in a 96 well plate. After 18 hours of incubation post-seeding, we added Bexarotene to corresponding wells to a final concentration of 25 uM to be incubated for 5 hours. We also used tBHQ at the final concertation of 100 uM and H_2O_2 1mM as a positive control. Cells were then washed with HBSS and incubated in presence of DCF-DA (25uM) for half an hour. After washing, 200uL of HBSS was added to each well, and plates were read at 485nm and emission wavelength of 530nm.

2.15. Statistical Analyses

All statistical analysis were performed using GraphPad Prism v 8.0, using a general linear statistical model as defined in each section. The error bar represents mean ± standard error of the mean (SEM). The statistical significance of p-value is designated with an asterisk (*), p-values: *$p < 0.05$, **$p < 0.01$, ***$p < 0.001$ and ****$p < 0.0001$.

3. Results

3.1. Bioinformatics Analysis Identifies BRF2 as a Promising Target in Cancer

We identified BRF2 as a potential cis-associated driver gene in breast cancer by performing copy number-altered network analysis[2]. Further examination of the literature revealed that aberrations in this region have been identified in breast tumors, correlating with metastatic relapse within one year [52,53]. To further validate this, we performed pan-cancer analysis on BRF2 expression levels and copy numbers using TCGA datasets. Comparison of RNA Seq data of gene expression levels in normal and tumor tissues in 32 cancer types reveals that BRF2 is significantly overexpressed in many tumor types, including malignancies of breast, lung, liver, and kidney (Fig 1A). In many cancers, such as esophageal squamous cell carcinoma, adrenocortical carcinoma, invasive breast carcinoma, NSCLC, bladder carcinoma and sarcoma, *BRF2* is often amplified and/or gained through copy number alterations (Sup fig 1A). Analysis of TCGA data in lung cancer depicts amplification/copy number gain in lung cancer, squamous cell carcinoma, and adenocarcinoma by 32%, 41%, 23%, respectively (Sup fig 1B-D). Verification of BRF2 against an independent dataset of 597 PAM50-subtyped breast tumors showed that BRF2 was upregulated, gained, or highly amplified in 37% of cases of TCGA, with copy-number amplification strongly correlating to mRNA upregulation in a substantial subset within each of the PAM50 subtypes (Sup fig 1E)[54]. Furthermore, METABRIC dataset shows 14% amplification in breast cancer across 2509 patients (Sup fig 1F). Analysis of 180 patients and 237 samples from the Metastatic Breast Cancer Project reveals 32% of metastatic breast cancers exhibit amplification and upregulation of BRF2 (Sup fig 1G). Correlation

 doi:10.20944/preprints202012.0770.v2

with survival data from these patients showed a significant association of BRF2 upregulation with poor survival, particularly in ER-positive tumors (Sup fig 1H). Notably, we found that *BRF2* amplification was mutually exclusive to loss of *BRCA1* and *BRCA2* in breast tumors both in TCGA and METABRIC data sets (Sup fig 1E,F). Mutual exclusivity of BRF2 amplification and BRCA1/2 loss was also observed in breast cancer cell lines in CCLE database (Sup fig I). *BRCA1* and *BRCA2*-associated tumors are defective in homology-directed DNA double-strand break (DSB) repair. *BRF2* amplification is rarely seen in the context of DNA damage repair deficiency. We have previously shown that BRF2 is upregulated in a number of breast cancer cell lines compared to near normal mammary epithelial lines and breast cancer cell lines with high BRF2 expression are dependent on it for cellular viability [2]. This analysis suggests that BRF2 is a potential therapeutic target in multiple cancers, including breast cancer.

Preprints (www.preprints.org) | NOT PEER-REVIEWED | Posted: 16 July 2021 doi:10.20944/preprints202012.0770.v2

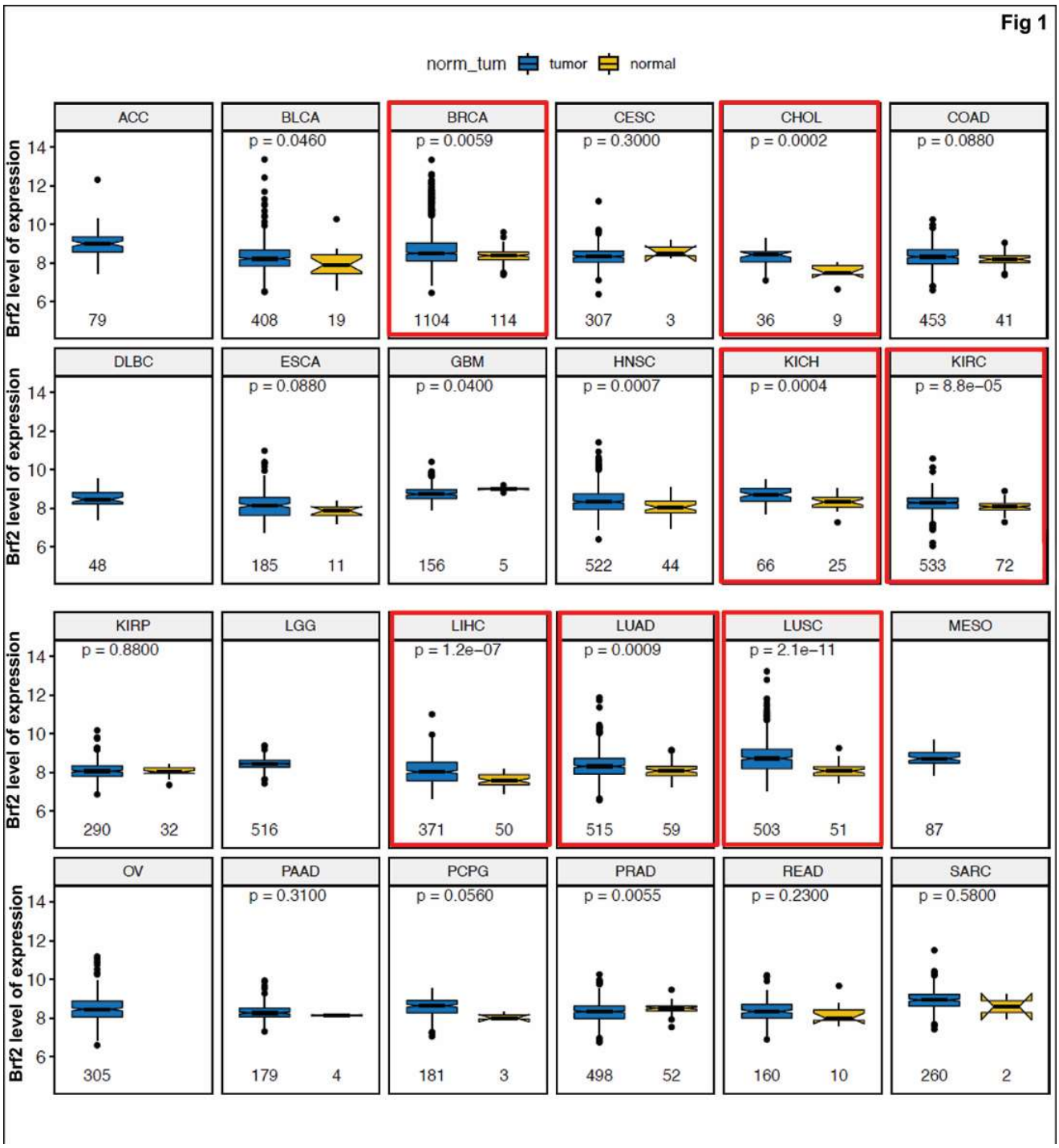

Figure 1. BRF2 elevated expression in multiple tumors. Comparison of gene expression levels in normal and tumor tissues in 24 cancer types. All data in these box plots are from The Cancer Genome Atlas (TCGA) RNAseq datasets. The box plots compare mRNA expression levels for the indicated gene (y-axes) between tumors and matched adjacent normal tissues (x-axes) of 24 cancer types. The abbreviations in the grey bars on top refer to the cancer types. Sample sizes (n) are shown below each box. Normal samples are missing for a few cancer types. The p values were calculated using the (unpaired) Mann-Whitney U test. (For Cancer type abbreviations see the supplementary data).

 doi:10.20944/preprints202012.0770.v2

Next, we analyzed the correlation between *BRF2* expression and 18 features (measures) of genomic instability, a hallmark of cancer. These analyses revealed that there are no strong correlations between the expression of *BRF2* in breast cancer dataset and selected features of genomic instability (Sup fig 2A-R).

We next investigated a possible link between BRF2 expression and cellular signaling pathways, as well as immunoregulation and tumor infiltration. Analysis of 12 different signal transduction pathways focusing on breast cancer identified a weak positive correlation between BRF2 expression and mTOR signaling (r=0.1728, p=1.9e−06, n=75); cell cycle regulation (r=0.1133, p=0.0018, n=753); stemness (r=0.1303, p=1.9e−05, n=1072); proliferation score (r=0.0856, p=0.0051, n=1072) and hypoxia score (r=0.1513, p=4.6e−07, n=1100) compared to other signaling pathways tested in breast cancer, including receptor tyrosine kinase (RTK), PI3K/Akt, Ras/ MAPK, epithelial-mesenchymal transition (EMT), apoptosis, chemosensitivity, autophagy, neoantigens, cancer testis antigens, and DNA methylation (Sup fig 3A-D). Finally, the levels of tumor-infiltrated immune cell types showed a marginal correlation between BRF2 expression with regulatory T cells (Tregs) (r=0.0875, p=0.0118, n=828); CD8+ T-cells (r=0.0715, p=0.0189, n=1078); T Cells Follicular Helper (r=0.0488, p=0.1118, n=1064) and activated NK cells (r=0.0924, p=0.0117, n=744) in breast cancer, using a tumor immune cell estimation resource (Sup fig 4). In conclusion, there is a limited correlation between *BRF2* expression and cancer hallmarks, signaling pathways, and immune markers. However, its amplification is mutually exclusive to DNA repair defects in breast cancer, suggesting that overexpression of *BRF2* may result in DNA damage repair deficiencies.

3.2. Evaluation of the Role of BRF2 in the Regulation of DNA Damage Response Pathway Utilizing Normal Mammary Epithelial Cells and Breast Cancer Lines

Given the possible link between overexpression of *BRF2* and DNA damage repair (DDR) deficiencies in tumors according to bioinformatics data, we aimed to investigate the possible role of BRF2 in the regulation of DDR experimentally. Excess ROS causes severe damage to cellular macromolecules, especially proteins and DNA. ROS is known to activate DNA damage response signaling via induction of DNA damage. BRF2 senses oxidative stress[1], and upon exposure to oxidative agents, BRF2-depleted cancer cells undergo oxidative stress-induced cell death, but normal cells avoid this through upregulation of selenoproteins. Therefore, we suspect a relationship exists between DDR signaling and BRF2. Exposure of MCF10A cells, a near normal mammary epithelial cells line derived from human fibrosarcoma, to different doses of γ -irradiation showed a marked increase in BRF2 expression, when harvested 1 hr after exposure (Fig. 2A). γH2AX, the biomarker for DSBs and p53-S15 and pKap1 (S824) phosphorylation, a downstream substrate of ATM/ATR, indicated the level of DNA damage induction in the cells. Also, we detected a robust increase in BRF2 within 1 hour of exposure to 0.5 Gy IR, which was more efficient than other markers of DDR signaling, including γH2AX and p-Kap1 (Fig. 2A). Further, a time-course experiment after exposing cells to 6 Gy IR revealed that BRF2 induction was very rapid and persisted over 6 hours in MCF10A (Fig. 2B). However, this increase is not mediated by an increase in mRNA levels of BRF2 (Fig. 2C). Similarly, in breast cancer lines, MDA-MB-231 and SUM159PT, using a longer time course of up to 24h, we found similar rapid and persistent upregulation of BRF2 upon DNA damage (Fig. 2D,E). Moreover, we found a robust stabilization of BRF2 that correlated with an increase in γH2AX in MCF10A cells treated with Tert-butylhydroquinone (tBHQ), the major metabolite of butylated hydroxyanisole, which induces an antioxidant response through the redox-sensitive, the nuclear factor-E2-related factor-2 (NRF2) transcription factor (Fig. 2F). NRF2 is a transcription factor that regulates the expression of antioxidant proteins and protects against oxidative damage[55]. This experiment further links BRF2 to DDR through the induction of oxidative stress. Additionally, we used the chemotherapeutic drug cisplatin as another DNA damage-inducing treatment, the concentration of drug used and length of exposure did not generate reactive oxygen species (data not shown),

Preprints (www.preprints.org) | NOT PEER-REVIEWED | Posted: 16 July 2021 doi:10.20944/preprints202012.0770.v2

which ionizing radiation is known to cause. BRF2 is upregulated following cisplatin treatment (Fig. 2G), which implies a link between DNA damage induction and BRF2 upregulation. Notably, after cisplatin treatment, we did not see changes in the level of oxidative stress marker, NRF2 (on the contrary a slight decrease is evident at 6 hrs) under the same experimental conditions. This supports a link between BRF2 upregulation and DNA damage induction although we cannot entirely rule out the possibility that BRF2 upregulation is triggered by cisplatin-induced oxidative stress.

Furthermore, we found that knocking down BRF2 using siRNA (MCF10A cell) causes an increase in baseline and IR-induced DNA damage, which was assessed by immunoblotting for γH2AX, however, no difference was observed in IR-induced induction of pKAP1 (S824), a direct substrate of ATM signaling (Fig. 2H). Likewise, the γH2AX clearance kinetic after IR-exposure was also markedly delayed when MCF10A cells were stably BRF2-depleted using shRNAs (Fig. 2I, J). Collectively, these data suggest a potential role for BRF2 in the regulation of DNA damage repair, given BRF2-depleted cells show persistent DNA damage.

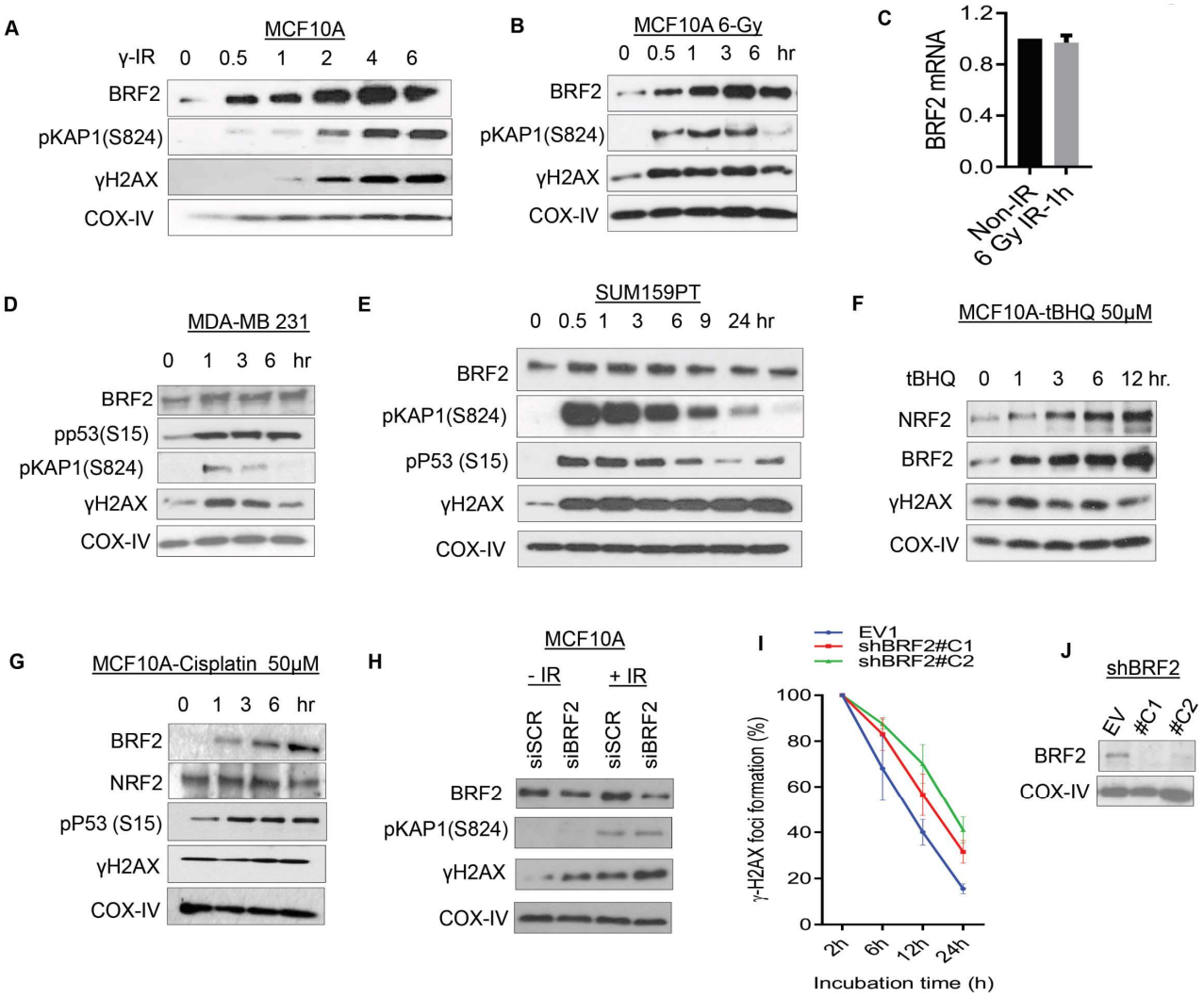

Figure 2. BRF2 is a potential DNA damage regulatory gene. (A) The dose response of BRF2 and other DNA damage response (DDR) related proteins in MCF10A after exposure to indicated dose of ionizing radiation (IR). (B) Time course of BRF2 expression following 6 Gy IR in MCF10A. (C) BRF2 mRNA expression in MCF10A post 1 hr exposure to IR (6 Gy). (D-E) Time course of BRF2

 doi:10.20944/preprints202012.0770.v2

expression following 6 Gy IR in breast cancer cell lines: (D) MDA-MB-231 and (E) SUM159PT. (F, G) Expression of BRF2, NRF2 and other DDR related proteins in MCF10A cells treated either with (F) 50μM tBHQ or (G) 50μM cisplatin at indicated time points. (H) Effect of BRF2 knockdown using siRNA on DDR signaling proteins (pKAP1(S824) and γH2AX) in MCF10A cells with and without IR exposure (6 Gy, post 6 hr). (I) γH2AX foci clearance assays were evaluated after exposure to 2 Gy IR in MCF10A cells over the time course of 24 hr. (J) Immunoblot shows the expression of BRF2 in empty vector (EV) and two different BRF2 knockdown clones (C1, C2) established in MCF10A, COX IV serves as a loading control.

3.3. Targeting BRF2 to Interrupt its DNA Binding.

Given the upregulation of BRF2 in cancer and our finding indicating its link with DNA damage repair, we aimed to target BRF2 by repurposing available drugs. BRF2 interacts with TBP and this complex can bind to DNA[1] (Fig 3A). The structure of BRF2 consists of a Zn ribbon, N/C cyclin repeats, and an arch, which binds the C-terminal and TBP anchor domains to the rest of protein (Fig 3 B, C). Initially, we attempted to target different available pockets of this protein for inhibiting its function, particularly Cysteine 361 (C361) which is considered as an oxidative stress switch in BRF2[1]. Sup Table 1 lists the drugs from Drug Bank and NCI which showed the best energy binding affinity, and Sup. Fig. 5 shows the architecture of these drugs at the C361 binding site according to the molecular docking. However, the molecular dynamics (MD) simulation for all of these drugs in the pocket as well as the binding site to DNA failed to demonstrate a stable bond (data not shown).

Given the difficulty in targeting BRF2 at C361 site, alternatively, we aimed to inhibit the BRF2–TBP binding complex. For this, we extracted BRF2 structure from PDB using 4ROC pdb ID which in this structure, BRF2 is in complex with TBP (Fig. 3D). Then, we used MD simulation to investigate the stable form of BRF2 in free state. A 100-ns (100,000 ps) MD simulation was performed to investigate the dynamic stability of free BRF2. The Root-Mean-Square Deviation (RMSD) was applied to compare the initial and final structural conformations of a protein backbone. During the course of the simulation, the relative stability of the protein to its initial conformation is determined by the RMSD value, where the fewer value is indicative of the greater stability. In order to evaluate the stability of both systems, the RMSD value for the Cα backbone was calculated during 100 ns. The RMSD profile indicated that during the initial periods of simulations, BRF2-free structure deviated considerably from the X-ray structure in the complex form[1]. The RMSD curves showed that the backbone trajectories of free-BRF2 structure were stable and reached equilibrium after the first 30,000 ps of the simulation, which ranged between 8 and 9 Å (Fig. 3E). Also, our 3D-structural analysis showed that at the end of the MD simulation, domain 2 (BRF2-CTD) of the protein rotated clockwise (Fig. 3F, Video 1). This conformational change in BRF2 after binding TBP is an important feature that might play a key role in binding to DNA. Therefore, we aimed to investigate the change of conformation in more detail.

Preprints (www.preprints.org) | NOT PEER-REVIEWED | Posted: 16 July 2021 doi:10.20944/preprints202012.0770.v2

Fig 3

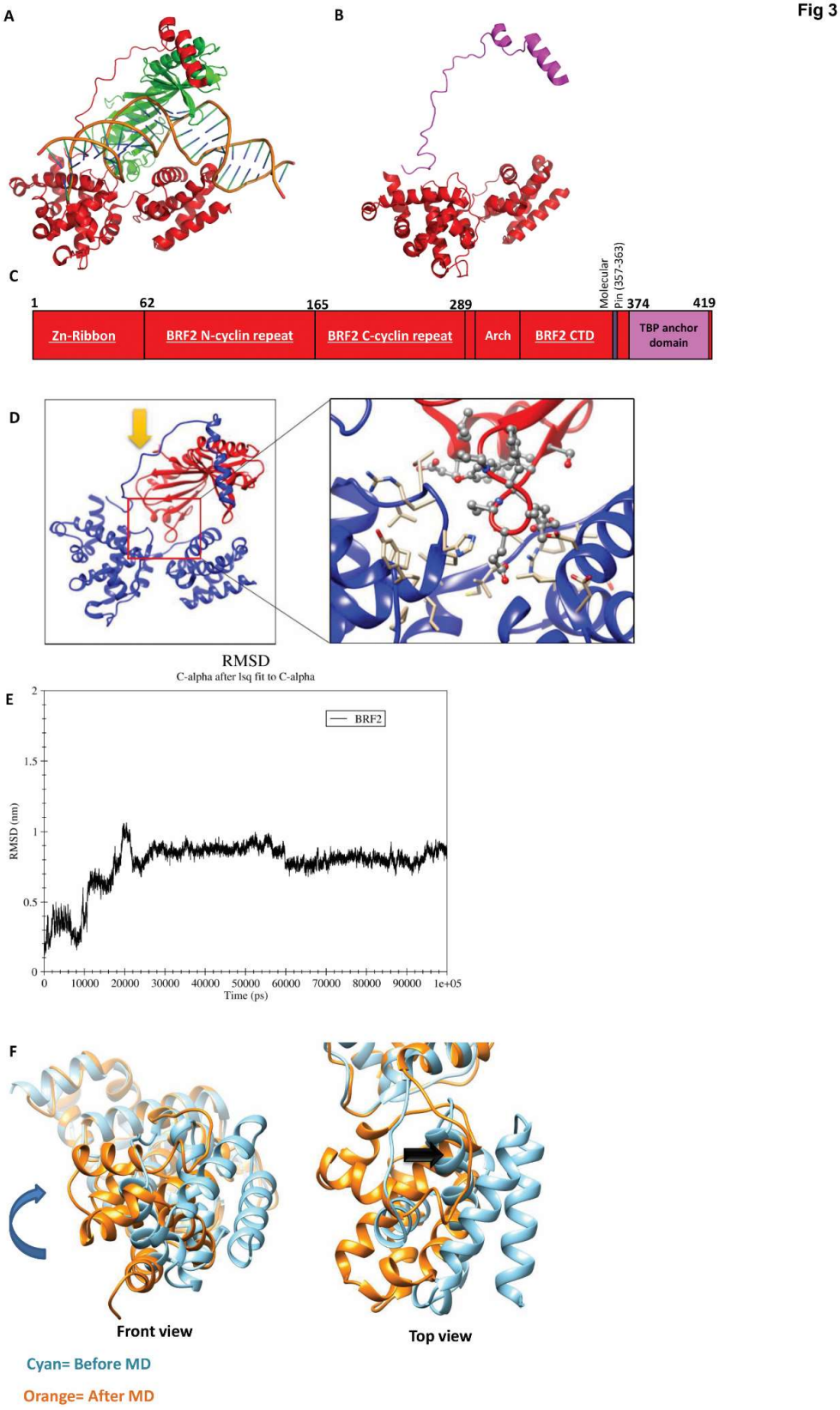

Figure 3. BRF2 structure and conformational changes. (A)The structure of the BRF2 in complex with TBP and DNA. (PDBID: 4ROC). (B) The structure of BRF2. (PDBID: 4ROC). (C) The schematic

 doi:10.20944/preprints202012.0770.v2

representation of BRF2 domains. (D) Binding site of TBP on the surface of BRF2 (PDBID: 4ROC). (E) RMSD plot of free-BRF2 during the 100 ns MD simulation by GROMACS. The figure is a representative image of at least three independent repeats. (F) Structural changes of BRF2 at the end of MD simulation. Cyan: Before MD and Orange: After MD. (See more details in Sup Video 1).

3.4. Principle Component Analysis (PCA) and Free-energy Landscape

For further evaluation of BRF2 conformational changes after binding to TBP during the MD simulation, principle component analysis (PCA) was carried out [56,57]. Fig 4A represents a plot of the eigenvalues obtained from the diagonalization of the covariance matrix of the Cα atomic fluctuations. The reduction in the eigenvalue amplitude indicates a shift from concerted motions to more constrained, localized fluctuations. This analysis suggested that the first two eigenvectors obtained from PCA can account for a higher percentage of the total motions in all simulations. As seen in Fig. 4A, the properties of motions for BRF2 described by the first two PCs are different.

To better understand the conformational changes of BRF2 protein at the free state, the conformational spaces of BRF2 were generated to gain significant information by using projections of MD trajectories on the first two PCs. Also, to deeply understand the motions, the displacements of eigenvector1 and 2 were calculated (Fig. 4B). As shown in Fig. 4B, the overall motion of the BRF2 protein has a different subspace of structures during 100 ns MD simulations, especially in PC1 mode. Based on Fig. 4B, the protein visits three conformational clusters in PC1. The root mean square fluctuation (RMSF) analysis of PC1 showed that these clusters correspond to enhanced displacements in the regions of 1-30, 70-95 and 115-130 residues (Fig. 4C).

For studying the differences in motion behaviors between the PC1 and PC2 modes, two porcupine plots are displayed in Fig. 4D which employ the first and second eigenvector using the VMD software. The direction of the arrow is an indicator of the collective motion direction, and the length of the arrow scales the strength of the movements. Based on this figure, the conformation of free BRF2 is different from TBP-DNA-BRF2 complex form of this protein.

In order to determine the low-energy basins (minima) and stability of the protein explored during the simulation, the free energy landscape (FEL) values of BRF2 were constructed using the projections of their own first (PC1) and second (PC2) eigenvectors (Fig. 4E). The energy minima and energetically favored protein conformations are shown in dark blue spots, and the unfavorable conformations are indicated in yellow spots. The shallow and narrow energy basin observed during the simulation showed the low stability of BRF2. Based on this figure, BRF2 showed a cluster consisting of two connected energy minima basins close to each other.

Preprints (www.preprints.org) | NOT PEER-REVIEWED | Posted: 16 July 2021 doi:10.20944/preprints202012.0770.v2

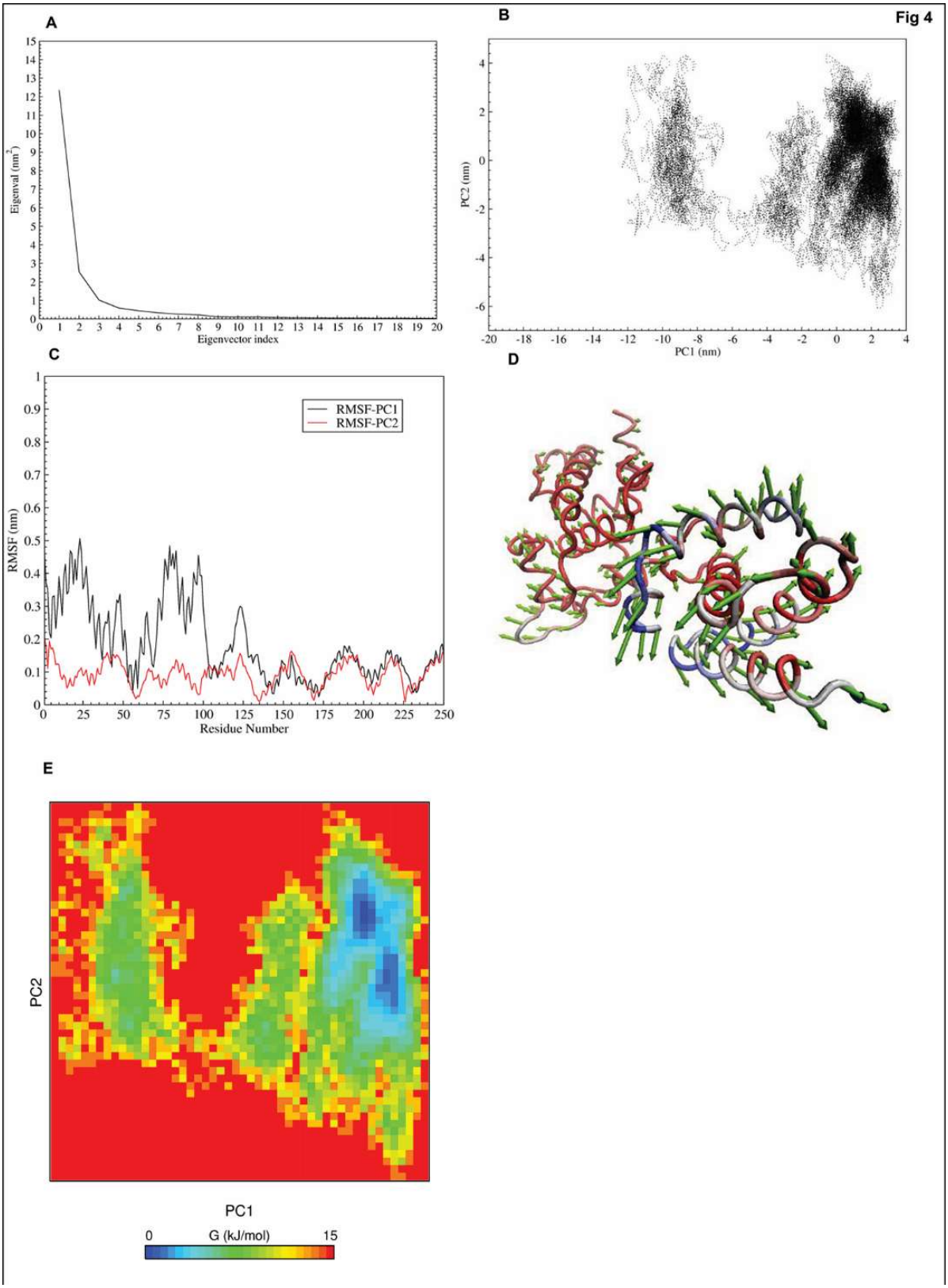

Figure 4. Confirmation of BRF2's conformational changes by PCA method. (A) The plot of eigenvalues obtained from the Cα covariance matrix built from MD trajectories. (B) Principal Compo-

Preprints (www.preprints.org) | NOT PEER-REVIEWED | Posted: 16 July 2021 doi:10.20944/preprints202012.0770.v2

nent Analysis of BRF2 protein. (C) Residue based mobility plot of BRF2 in mode 1 and 2. (D): Porcupine plots of the PCA analysis for PC1 depicting the movement and altitude of the C-alpha atoms throughout the 100 ns simulation. (E): Free energy landscape of BRF2 protein.

3.5. Targeting BRF2–TBP Binding Using Drugbank Ligands

After identifying the conformational changes of BRF2, we used the correct conformation for *in silico* studies. To interpose BRF2-TBP binding complex by an effective drug from the Drug Bank database, we performed a virtual screening using molecular docking with the rigid protein and flexible ligands. The optimized output structure of BRF2 after MD was utilized as a target for the virtual screening phase, and the top drugs were ranked based on the lowest binding-energy value. The list of drugs (Table 1) and the architecture of binding has been shown in Fig. 5 and Sup fig 6. As shown in table 1, docking results represent that the binding energy of Phthalocyanine to BRF2 is higher than the other ligands (-10.5 kCal/mol). Therefore, the stability of this ligand was analyzed during the MD simulation. The condition of our MD simulation was explained in the material and method section. As shown in sup fig 7A (0 ns) and sup fig.7B (after 8 ns) the ligand separated from the binding site, and moved out of the cavity (direction of the ligand movement indicated by arrow). Nevertheless, Phthalocyanine, the large aromatic macrocyclic compound, had the lowest energy binding; this compound was not stable after simulation. As can be seen in docking representations (Fig 5), the second hit was the retinoic acid receptor gamma agonist (CD564), which can fit properly at the pocket of the site.

Therefore, we chose CD564 for simulation and performed MD for both BRF2 and drug (Fig. 6A, Sup Video 2). The RMSD value of the ligand was stable until 16,000 ps followed by a sharp rise from 0.6 to 0.9 Å with fluctuations around this value until the end of the simulation. The analysis in Fig 6A indicates that the RMSD value of the protein reached equilibrium and oscillated around 0.2 nm for approximately 7,000 ps of simulation time. This evidence clearly indicates that the whole system was stable and equilibrated and that CD564 is a suitable compound to inhibit the binding site of BRF2 and TBP. The final structure of the complex and ligand binding site is shown in Figure 6B-D and Video 2.

Table 1. Fifteen top-ranking docked compounds, binding energies.

Target	Best Ligands	Binding Energy (kcal/mol)	Function
Protein: BRF2 PDB: 4ROC	Phthalocyanine	-10.5	An under investigation drug in clinical trial NCT00103246 for treatment of patients with Skin Cancer, Bowen's Disease, Actinic Keratosis, and Stage I / II Mycosis Fungoides.
	CD564	**-10.1**	**Under investigation**
	Alectinib	-9.9	A second-generation oral drug that selectively inhibits the activity of anaplastic lymphoma kinase (ALK) tyrosine kinase.
	Zk-806450	-9.8	Under investigation
	SR11254	-9.7	Under investigation
	BMS184394	-9.7	Under investigation
	AZD-5991	-9.7	An under investigation in clinical trial NCT03218683 for relapsed or refractory hematologic malignancies.
	Bemcentinib	-9.6	Bemcentinib has been investigated for the treatment of Non-Small Cell Lung Cancer.
	Pranlukast	-9.6	A cysteinyl leukotriene receptor-1 antagonist which antagonizes/ reduces bronchospasm caused in asthmatics, by an allergic reaction to accidentally or inadvertently encountered allergens.
	DB07456	-9.5	Under investigation

Preprints (www.preprints.org) | NOT PEER-REVIEWED | Posted: 16 July 2021 doi:10.20944/preprints202012.0770.v2

TMC-647055	-9.5	TMC647055 has been used in trials studying the treatment of Hepatitis C, Chronic Hepatitis C, Hepatitis C, Chronic, and Chronic Hepatitis C Virus.
Aleplasinin	-9.5	Aleplasinin has been investigated in Alzheimer Disease.
Orvepitant	-9.5	Orvepitant has been used in trials studying the treatment of Depressive Disorder, and Posttraumatic Stress Disorder (PTSD).
Galicaftor	-9.4	An under investigation in clinical trial NCT03540524 With or Without GLPG2737 in Patients With Cystic Fibrosis).
Baloxavir	-9.3	An under investigation drug in clinical trial: NCT04327791 in combination therapy with Baloxavir / Oseltamavir 1 for patients with influenza.

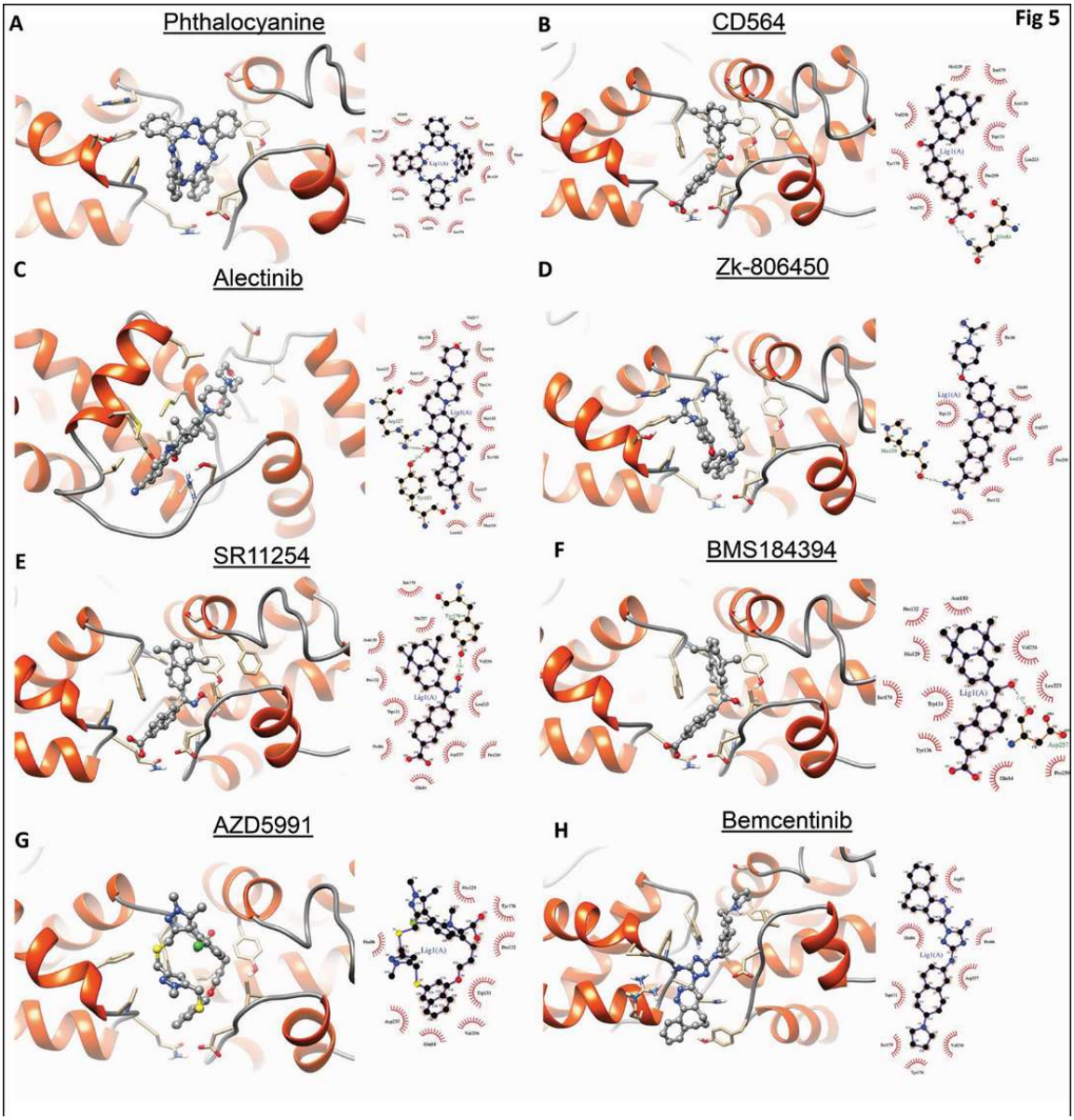

Figure 5. Results of the 8 top-ranking docked compounds, with BRF2 protein according to the binding energies. **(A-B)** show the surface views of the two best-ranked ligands according to docking and **(C-J)** show the protein-ligand 3D and 2D interaction diagram of the protein ligand complex.

 doi:10.20944/preprints202012.0770.v2

3.6. Thermodynamic Parameter Calculations

One of the most important analyses after MD is the calculation of binding free energy (ΔG). Using g_mmpbsa (Molecular Mechanic/Poisen-Boltzman Surface Area, MMPSA) software and molecular dynamic simulations, we calculated the relative binding free energy. Four hundred extracted snapshots were used to calculate the binding energy. The binding free energy and its related components acquired from the MM/PBSA calculation of the ligand-BRF2 complexes are listed in Table 2. The results showed that the ligand possessed a high negative binding free energy value of -412.059 kJ/mol. Further evaluation showed that electrostatic energy contributed most to the protein binding to the ligand, where the carboxyl group bound to Arg81 with electrostatic interactions, causing the total electrostatic energy to become negative (Fig. 6E). Our analysis showed that the Binding energy of this residue is -24.29 kJ/mol. Also, the binding energy for other residues is available in Sup7c. Van der Waals interactions also played a critical role in this binding as $\Delta G_{solv\text{-}polar}$ was 197.664 KJ/Mol. The ΔG_{MMPBSA} was also indicative of strong, high-affinity binding between protein and ligand.

Table 2. Calculation of binding free energy (ΔG) and components of ligand binding energy at the site of binding.

(kCal/mol)	ΔG_{vdw}	ΔG_{elec}	$\Delta G_{solv\text{-}polar}$	$\Delta G_{solv\text{-}nonpol}$	ΔG_{MMPBSA}
Native	-163.389	-427.767	197.664	-18.567	-412.059

For calculating absolute ligand-protein complex binding energy.US method was used at this step and the ligand pulled 2.5 nm from the binding pocket. The binding free energy (ΔG) was calculated by taking the difference between the highest and lowest value of the PMF graphs. This unbinding process requires −10.29 kcal/mol energy to dissociate the ligand. As shown in Fig. 6E, the ligand has carboxyl and aromatic ring sub-structures. Based on this LigPlot, the ligand has strong interactions with surrounding residues, especially TRP131, PHE180, GLN84 and ARG81. The pulling simulation revealed that an extended stay inside the binding pocket was the result of interactions with several amino acids. During the dissociation process, we observed four energy minima (Fig 6F). The conformation of the mentioned four energy minima are shown in Fig 6G. at the conformation of 1a the carboxyl group of ligand makes hydrogen bond and electrostatic interactions with Tyr260 and Arg81, respectively. Also, rings 3 and 4 established pi-pi stacking and pi-slkyl interaction with Trp131 and Tyr176 respectively. At the second energy minimum (1b) the mentioned hydrogen and electrostatic interactions were broken, but the pi-pi and pi-alkyl interactions still were remained. At the third energy minimum (1c), the carboxyl group of ligand makes new electrostatic interaction with Lys181. At the fourth energy minimum (1d), the length of salt-bridge interaction between Lys181 and ligand reached from 2.71 to 4.58 Angstrom, so, the ligand started to come out from the binding cavity. The molecule again pulled continuously, and PMF graph attained equilibration at around ~3 nm distance. At this position, the molecule was entirely unbound and became solvent-exposed. Figure 6G and Sup video 3 represent the unbinding pathway of the ligand from the binding site.

Preprints (www.preprints.org) | NOT PEER-REVIEWED | Posted: 16 July 2021 doi:10.20944/preprints202012.0770.v2

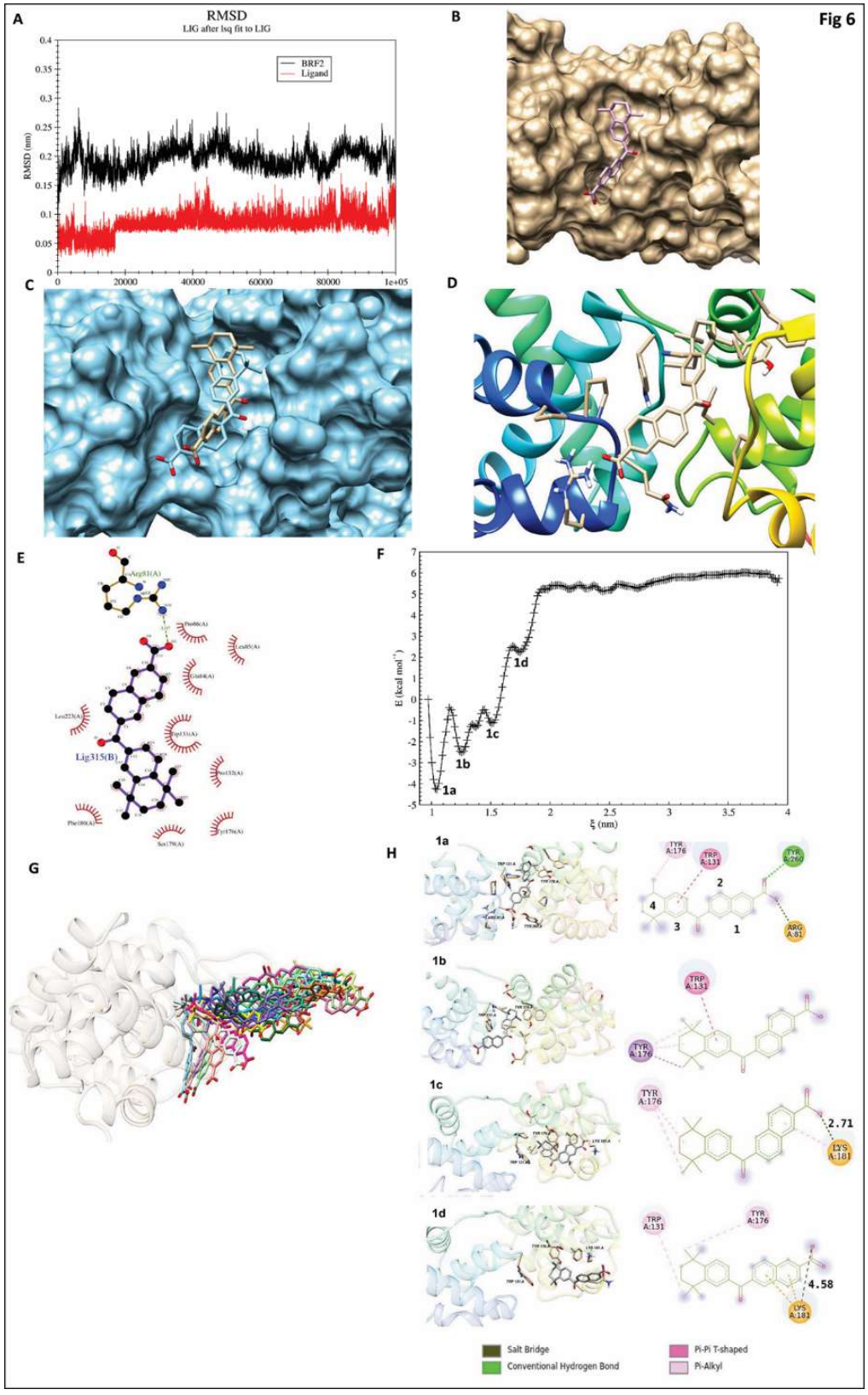

Figure 6. Molecular dynamic simulation. (A) RMSD of BRF2 (black) and ligand (red) during the 100 ns MD simulation. (B-D) Docked BRF2-ligand complex in different views. (B) surface view, (C), surface view shows the conformational changes of ligand before (khaki) and after (blue) of

 doi:10.20944/preprints202012.0770.v2

MD in the pocket (D) ribbon view. (E) LigPlot-generated snapshot of the ligand and residues in the active site. (F) The PMF graph obtained from US simulation, (G) unbinding pathway of ligand from binding site. (H) 1a, 1b,1c and 1d are the energy minimum obtained from US simulation.

3.7. Experimental validation of Drug

In order to experimentally validate drug efficacy, we searched for an available FDA approved drug most similar to CD564. According to the Drugbank inquiry, Bexarotene (Fig 7A) has more than 70% structural similarity score as well as similar function as a retinoid that activates retinoid X receptors (RXRs)[58]. Bexarotene (Targetin) is an approved anti-cancer drug for treatment of cutaneous T cell lymphoma (CTCL)[59]. To further examine whether this drug is as efficient as CD564, the geometry of Bexarotene in the binding site was initially studied by MD. Based on docking result, the binding energy of ligand at the binding site is equal to -8.8 kCal/mol. As shown in Fig 7B, the geometry of ligand at the binding site is similar to CD564.

The stability of the BRF2- Bexarotene (Bex) complex was analyzed during 100 ns MD simulation. The RMSD plot of this simulation shown in Fig.7C indicates the RMSD value of protein increased gently until 30 ns of simulation. Then, the RMSD value suddenly increased to 0.5 nm after 36 ns, which is indicative of significant conformational changes in the complex (Fig.7C). Then, the RMSD value decreased again and reached approximately 0.3 nm at the end of the simulation. Based on Fig.7C, there is minimal variation in the RMSD of the ligand during MD simulation. As shown in Fig.7C, significant conformational changes were observed in the protein. For better visualization purpose, we colored the residue numbers 83-84 at two conformations (before MD (green) and after-37ns (cyan)) (Fig.7D). Based on this figure, after 37ns, the left domain of protein rotated upward. Also, a similar situation in the ligand can be seen. However, at the end of the simulation, the conformation of protein has returned to its normal form (Fig.7E). These data show that Bex is a potential candidate for the experimental validation.

After initial *in silico* confirmation, we aimed to identify the drug sensitivity response based on BRF2 gene expression using the genomics of drug sensitivity in cancer (GDSC) database[60]. The IC50 of Bex correlated negatively to the expression of BRF2 among the breast cancer cell lines (the threshold of expression set to -2 to 2) (Fig 7 F) unlike the other available drugs on the list (Alectinib and AZD5991) (Sup 7 D,E). This is indicative of the potential efficacy of Bex with increasing BRF2 expression in the indicated cancer setting.

To experimentally validate the effect of Bex on BRF2-TBP binding complex, we treated MCF7 cell line control (scrambled siRNA) and BRF2 -depleted (BRF2 specific siRNA) with either DMSO or the drug. BRF2-depleted cells showed a decline in cell viability (MTS assay) compared to control MCF7 cells which is indicative of the dependency of cells on this essential gene. However, the further reduction of cell viability was observed in both Bex- treated scramble and BRF2-knockdown cells, suggesting that antiproliferative effect of Bex observed in this line is non-selective for BRF2 expression (Fig 7 G). Western blotting of drug-treated MCF7 cells did not show a significant decrease in BRF2 expression compared to untreated cells. Consistent this we failed to see significant induction of cell death as evident by cleaved PARP in Bex treated MCF7 (Fig 7 H), which was clearly evident after siRNA-mediated depletion of BRF2.

We also used doxycycline induced CRISPR/iCas9 mediated knockdown of BRF2 in HeLa cells. We could not find significant changes in BRF2 expression level after Bex treatment in Doxycycline negative as control and Doxycycline induced (knockdown of BRF2 Hela Cells. However, Bex treatment of control (Dox-) and BRF2 knockdown cells (DOX+) resulted in a dramatic decline in oxidative stress agent, tBHQ induced expression of BRF2 (Fig 7 I). Consistently, the proliferation assay showed a dramatic reduction of cell proliferation in either control (Dox-) or BRF2 knockdown cells treated with both tBHQ and Bex (Fig 7J). Next, we aimed to assess whether this effect is due to the role of Bexarotene in quenching ROS generation by tBHQ. Therefore, we treated the cells with tBHQ with or without pretreatment with Bexarotene. The results showed that the pre-treatment

Preprints (www.preprints.org) | NOT PEER-REVIEWED | Posted: 16 July 2021 doi:10.20944/preprints202012.0770.v2

of cells with Bexarotene significantly reduced ROS formation with and without tBHQ treatment (Fig 7K).

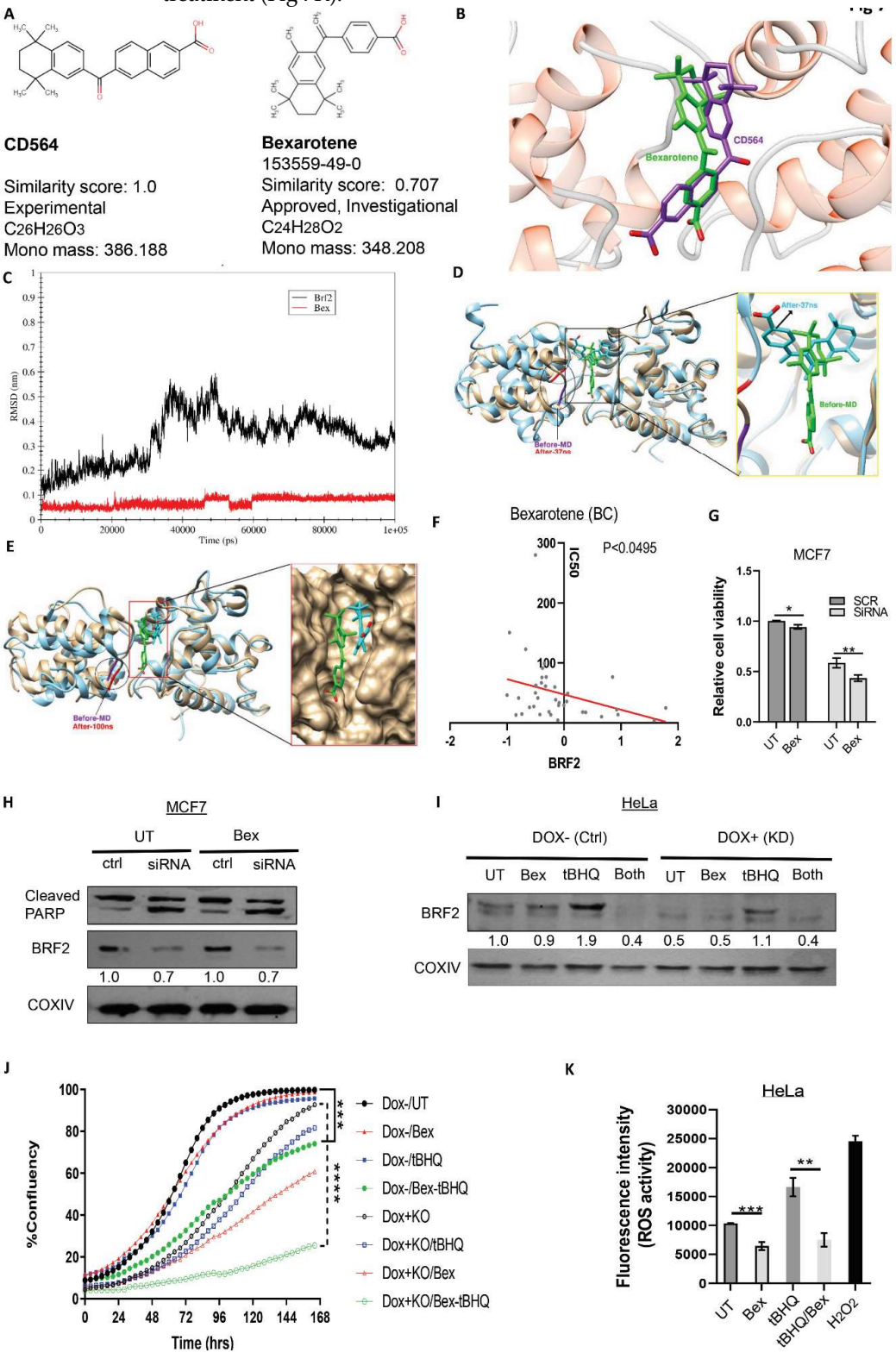

Figure 7. Bexarotene (Bex) effect on BRF2. (A) Two-dimensional structure, chemical formula and similarity score between CD564 (left) and Bex (right). (B) Docked BRF2-ligand complex for CD564 (purple) and Bex (green). (C) RMSD plot for BRF2-Bex during 100 ns MD simulation. (D) Docking shows 2 conformations of drug (before MD: green, and after 37 ns:

 doi:10.20944/preprints202012.0770.v2

cyan. (E) Docking shows 2 conformations of drug (before MD: green, and after 100 ns: cyan. notice that the conformation of drug has returned to its normal form. (F) Correlation between IC50 of Bex and BRF2 expression in breast cancer cell lines (threshold of expression is set between -2 to 2). (G) Relative cell viability comparison of untreated (UT) and drug treated (Bex) between Scramble (black) and siRNA mediated knockdown of BRF2 (Grey). (H-I) Immunoblot shows expression (H) of cleaved PARP and BRF2 in scrambled (Ctrl) and siRNA mediated knockdown of BRF2 in MCF7 cell line, (I) BRF2 expression in untreated (UT), drug treated (Bex), tBHQ induced oxidative stress (tBHQ), Bex plus tBHQ treated (Both) in CRISPER/inducible cas9 mediated knockdown of BRF2 in HeLa cell without Doxycycline (Dox negative/Ctrl) and with 2 μg/ml Doxycycline (Dox positive/Knockdown of BRF2), COX IV serves as a loading control and normalized quantification of BRF2 bands has been shown below each band. (J) Proliferation assay shows the percent of confluency of HeLa cell without Doxycycline (Dox -/control) and with 2 μg/ml Doxycycline (Dox +/ BRF2 knockdown) for each indicated condition. (K) ROS activity of Hela cell for indicated conditions (Untreated (UT) cells, Bexarotene (Bex) treated cells, tBHQ treated and both Bex + tBHQ treated. H_2O_2 serves as a positive control) across the indicated time. For all calculations, data represented mean ± SD and Data were measured in duplicate across 3 independent experiments. Student's t-test performed, *P < 0.05, **P < 0.01, ***P < 0.001, ****P < 0.0001.

4. Discussion

It has been proposed that targeting transcription factors may offer a therapeutic option with lower toxicity and increased efficacy than current chemotherapy drugs, which opens opportunities for novel drug-development approaches[61]. Classical chemotherapy agents targeting DNA integrity and cell division have the potential to give rise to secondary malignancies. Current strategies target oncogenic molecules or signaling pathways that tumor cells are dependent on for growth and survival. This phenomenon is known as oncogene addiction. However, there is emerging interest in targeting multi-component cellular machinery that is not directly involved in growth and proliferation to maintain the malignant properties that contribute to tumorigenicity (non-oncogenic addiction)[62,63]. BRF2 and the other class III genes transcribed by Pol III are known as 'housekeeping genes', and their expression is required in all cell types for cellular viability. Housekeeping genes have been suggested as anti-cancer targets with therapeutic potential given the likelihood of reduced associated toxicity[64]. TFs are targeted by approximately 10% of all FDA-approved anti-cancer drugs[65]. However, most TFs are not targetable because of their localization, or because their components and subunits do not possess enzymatic activity, which is usually easier to target with specific drugs. Therefore, we endeavored to identify a mechanism by which BRF2 could be targeted. However, most of the accessible pockets and available domains in BRF2 were not targetable, and we could only target BRF2 and TBP binding sites to impair their DNA-binding capacity. The formation of a complex between various proteins has a key role in many biological processes, and consequently, preventing complex formation interrupts the associated processes. However, BRF2 plays a key role in protecting cancer cells against oxidative stress and our data additionally suggest that BRF2 plays a role in DDR regulation. Therefore, inhibition of this target can be more valuable than targeting other TFs or housekeeping genes.

Recently, there has been increased interest in targeting polymerases, such as the targeted destruction of the Pol I, to treat patients with advanced solid tumors, which ultimately expands therapeutic opportunities[66]. Notably, targeting components of Pol I using the selective inhibitor CX5461 to treat tumors with MYC amplification has shown selective killing of tumor cells through activation of non-canonical ATM signaling[67]. Additionally, different modes of action for CX5461 as TOPO isomerase II poison or G-quadruplex-mediated global DNA-damage induction have been proposed[68,69]. Regardless of the difficulties in targeting RNA polymerases and their associated regulators, the recent discoveries of drugs that are able to target these proteins underline their potential in the future of cancer therapy. Oncogenes such as MYC, or tumor-suppressors such as RB and p53, are multiple regulators of Pol III and Pol II. Furthermore, these common regulators have a global effect on Pol III, which makes it more complex to assign a specific gene contribution to Pol III deregulation. Due to its pivotal role in cell growth, proliferation and tumorigenesis, Pol III activity is tightly regulated by a series of activators and repressors.

 doi:10.20944/preprints202012.0770.v2

For example, the Pol III repressor MAF1 is negatively regulated by a series of phosphorylation events on seven different serine residues[70]. Similarly, RB and the RB-related family members repress Pol III activity and heightened levels of PolIII transcripts are implicated in accelerated growth associated with RB dysfunctional tumors[71,72]. The Casein Kinase 2 (CK2) is an extremely conserved kinase that plays pivotal role in many aspects of cell physiology; moreover, CK2 is often overexpressed in several human cancers[73]. Among its many substrates, CK2 also regulates several transcription factors and polymerases, including Pol III[74] and the TFIIIB sub-factor TBP[75]. Another kinase involved in Pol III phosphorylation is ERK. In response to mitogen activation, the mitogen-activated protein (MAP) kinase ERK regulates Pol III activity through direct binding and phosphorylation of BRF1[76]. The phosphatase PTEN plays a fundamental role in tumor suppression by inhibiting the PI3K signaling, and it is often mutated or lost in human cancers[77]. Moreover, PTEN represses the activity of Pol III by blocking the formation of functional TFIIIB complexes. Specifically, PTEN blocks the association between BRF1 and TBP: this inhibition occurs through the reduction of phosphorylation of BRF1 that induces the dissociation of TFIIIB[78].

Considering the vital role of TFs and their subunits in regulating oncogenic pathways, we performed a comprehensive bioinformatic analysis, correlation studies and literature review on the effect of BRF2 on signaling pathways. However, our analysis revealed that unlike Pol III transcript itself, BRF2 transcript is not linked to the above-mentioned signaling pathways. Notably, BRF2 mRNA expression in human tumors also did not correlate with any feature of genomic instability as an indicator of DNA damage (Suppl fig 3). This is supported by our *in vitro* data in human breast cancer lines (Fig 2), showing that the BRF2 protein levels are regulated after exposure of cells to DNA damaging agents, rather than at the transcript level. Thus, it is likely that BRF2 might be post-transcriptionally regulated by above-mentioned signaling pathways.

Next, we further characterized the relationship between BRF2 and DDR experimentally. BRF2 is a major oxidative stress regulator, and oxidative stress mechanisms can drive tumorigenesis[2]. A BRF2-regulated gene product, known as SeCys tRNA, is involved in the synthesis of selenoproteins. The main function of SeCys tRNA is to reduce reactive oxygen species (ROS) and maintain the cellular redox homeostasis through selenoprotein synthesis[1]. The absence or defective expression of selenoproteins induces apoptotic cell death. Studies have shown a high basal level of BRF2 expression in breast[2] and lung cancer[3], as well as in cancer cell lines such as HCC95 which are subjected to prolonged oxidative stress [4]. Therefore, it has been speculated that the high levels of BRF2 expression in cancer cell lines assists in maintaining sufficient expression of selenoproteins in order to detoxify ROS and preserve redox homeostasis. DNA damage induction is linked to oxidative stress, which can in turn cause further DNA lesions. It was conspicuous that in the investigated cancer cell lines and near-normal breast cell line (MCF10A), the expression of BRF2 was upregulated after ionizing radiation. We also used cisplatin as another DNA damage-inducing treatment as published reports from many laboratories have demonstrated DNA as a direct target for cisplatin toxicity [79–81]. The most revealing evidence has been hypersensitivity to cisplatin seen in DNA repair defective prokaryotic and eukaryotic cells. However, there are some reports that denoted the formation of reactive oxygen species depends on the concentration of cisplatin used and the length of exposure. In our in vitro experiments, cells were only transiently treated with cisplatin for up to 6 hrs, we did not detect any generation of reactive oxygen species after cisplatin exposure in our experimental condition assessed using DCFDA/H2DCFDA ROS Assay kit (data not shown). Thus, the cisplatin experiment represents DNA damage-inducing treatment to exclude BRF2 as possibly being activated by oxidative stress, which is triggered by radiation[81–84]. BRF2 demonstrates clear upregulation following cisplatin treatment, which implies a possible link between BRF2 and DNA damage induction. Additionally, the expression of NRF2 (a protein stimulated by oxidative stress[85]), was examined after cisplatin treatment and under our experimental conditions, no significant

 doi:10.20944/preprints202012.0770.v2

changes were detected. This strengthened the possibility of the link between BRF2 and DNA damage. While we were preparing the revised manuscript, the link between Pol III and DDR was reported where Pol III localizes to double-strand breaks (DSB) site and is required for the DNA repair [86]. Consistent with our findings, the authors reported an increase in chromatin levels of the Pol III-subunits in cells treated with the DSB-inducing agents [86].

After characterizing the potential role of BRF2 in DDR, we initially aimed to target C361 in BRF2, which is critical on/off switch of OS. However, according to molecular simulations, we failed to identify any effective drugs. Therefore, we concentrated on targeting the BRF2-TBP-DNA complex. However, after MD simulation, the high protein RMSD value along the trajectory indicated a significant change in the molecular structure had occurred. The stability of the protein after 30 ns, persisting at a value of approximately 1 nm, illustrated its stability after the large conformational displacement. Following this discovery, we used PCA to reveal the critical motions of a protein, as a confirmation for conformational changes. The PCA revealed the origin of the large conformational difference between the initial and final MD structures. This is supported by their different motion direction relative to each other. Analyzing residue displacements according to the projection of MD trajectories on the first and second components verified that larger displacements of some residues, located at the N-terminus of protein, make two conformations visiting different subspaces during MD simulations. This provided significant dynamics information involving conformational diversity of BRF2 protein in both the bound and free states. The free energy landscape (FEL) analysis provided intimate details about the stable conformation and energy minima. BRF2 FEL analysis showed two energy minima that represent the two conformations of protein (bound and unbound). Finally, the stable conformation of this step was used as a receptor structure to perform virtual screening.

A structure-based virtual screening method was used to select the ligand with a high binding energy value using the stable conformation of BRF2 before binding to TBP. Our analysis showed that the ligand has an acceptable binding energy value. The MD simulation method was used to study the stability of ligand at the binding site. RMSD plot confirmed that the protein and ligand are stable during the MD simulation. At the next step, the relative binding free energy of ligand to protein was calculated by the MMPBSA method. MMPBSA analysis showed that the non-polar solvation energy, van der Waals and electrostatic interactions (the most effective) contribute to the total interaction energy negatively. However, only the polar solvation energy contributes to the total free binding energy positively. Also, the interaction plot generated by ligplot showed that the carboxyl group at the ligand makes electrostatic interaction with Arg81 of protein. Collectively, using *in silico* approaches we have identified putative inhibitors of BRF2-TBP-DNA complex after the virtual screening of more than 3500 FDA approved or under clinical trial investigational drugs from Drugbank. We identified CD564 as a promising candidate that can create a stable binding interaction with the binding site of BRF2-TBP and consequently, interposes links DNA binding with the functionality of BRF2. We validated these results by using MD simulation where RMSD charts indicated the stability of bound and thermodynamic parameters verified by the binding energy. We finally, confirmed the CD564 binding to BRF2 by using molecular dynamics simulation.

Due to the limited availability of CD564, we queried similar FDA-approved drugs to examine the result. The FDA-approved drug, Bexarotene (Bex) had the best score (70% similarity) and therefore, it was chosen for primary *in silico* analysis. Being successful in binding and molecular simulation using docking followed by MD, we further validated the effectiveness of this drug experimentally. First, we found a negative correlation between the drug sensitivity and expression of BRF2 in breast cancer cell lines which indicates that this drug is more efficient when BRF2 expression is higher. However, Bex treatment did not impact BRF2 expression and slightly reduced proliferation of control and BRF2 depleted MCF7 cells without induction of cell death, suggesting that the anti-

 doi:10.20944/preprints202012.0770.v2

proliferative effect of Bex was independent of BRF2 expression. However, siRNA-based depletion of BRF2 in MCF7 led to a significant induction of cell death. Similarly, Bex treatment alone was unable to reduce BRF2 expression significantly in both Dox negative (control) and positive (BRF2 knockout cell) generated using CRISPR/iCas9 system. This was in line with our *in silico* data which showed the drug binds to BRF2 in certain conformation. Surprisingly, tBHQ could increase BRF2 level approximately 2 folds in both conditions. This phenomenon indicates that CRISPR/iCas9 system could not totally knockout BRF2 expression and upon treatment with tBHQ which generates oxidative stress, its expression increased. Due to polyclonal selection of this line, heterogeneous populations of cells might still express BRF2 to some extent even in Dox-positive lines which are indispensable for cell viability. Interestingly, Bex significantly reduced tBHQ -induced BRF2 upregulation in both control and BRF2 knockdown cells. Additionally, combined Bex and tBHQ challenge in these lines significantly reduced cell proliferation but not treatment with Bex or tBHQ alone. We hypothesized that the drug is only effective on a particular conformation of BRF2 before its binding to TBP. Therefore, this finding is in line with our hypothesis that the drug is not effective on the changed BRF2 conformation in complex with TBP, which exists in the cells. However, the newly synthesized BRF2 following oxidative stress induction in both conditions was inhibited by the drug. This scenario can confirm the anti-cancer effects of this drug in cancers with high oxidative stress that upregulate BRF2 expression. Yet, further experimental investigation is required to test the binding capacity of purified recombinant BRF2 protein to the drug which is out of the scope of this paper.

However, this drug can also modulate different cellular components and signaling pathways. Bexarotene is a retinoid X receptor (RXR) agonist which is FDA approved for treatment of cutaneous T cell lymphoma. As a therapeutic strategy, RXR agonisms have been investigated in other cancers. Specifically, Bexarotene downregulates the expression of inflammatory cytokines such as interleukin (IL) 6, IL-8, and monocyte chemoattractant protein-1[87]. Additionally in TNF-α stimulated human fibroblast-like synoviocytes, Bexarotene has been shown to downregulate the expression of matrix metallopeptidases (MMPs), upregulate the anti-inflammatory cytokines IL-4 and TGF-β1, and attenuate nuclear factor (NF)-κB and p38 mitogen-activated protein kinase (MAPK) signaling [87]. Given the role of BRF2 in reducing reactive oxygen species (ROS), we examined the specific role of the drug on the generation of ROS by oxidizing agent tBHQ and related ROS activity. We found that in our experimental condition Bex pretreatment could significantly reduce baseline as well as oxidant-tBHQ induced ROS levels. Anti-proliferative effect of the combination of Bex and tBHQ can be explained by a significant reduction in levels of BRF2. Our results suggest potential efficacy of Bex in reducing BRF2 levels in cells with a high-level of oxidative stress but future validations are required to investigate the detailed mechanism of drug action *in vitro* and *in vivo*.

5. Conclusions

In conclusion, we showed BRF2 as a potential therapeutic target in cancer by comprehensively analyzing publicly available Pan-Cancer data. We also discovered the regulation of BRF2 after DNA damage in breast cancer. Notably, using virtual screening on more than 3500 available drugs, we found inhibitors of the BRF2-TBP-DNA complex binding which were successfully validated by molecular docking, energy binding and MD simulation results. MD results revealed that BRF2 undergoes a conformational change after binding to TBP, which leads to changes in the available pockets. Using this structure, we found Bexarotene, an FDA approved drug, is a potential hit for the development of BRF2 specific inhibitors according to *in silico* analysis and negative correlation of drug sensitivity to BRF2 protein expression in GDSC database. Further experiments showed this drug inhibited proliferation of control and BRF2-depleted cells, suggesting that its anti-proliferative effects are not selective for BRF2 expression. Interestingly, Bexarotene reduced the oxidative stress-induced high level of BRF2 by reducing the cellular levels of

ROS generated. Overall, this research identified BRF2 as a promising cancer target; indicated the molecular changes in the architecture of this protein by binding to TBP; provided the potential hit compounds for this target followed by examining one of them experimentally as well as implying the new roles for BRF2 in DDR regulation.

Author Contributions: Conceptualization, BR, MM, AM, MK, KK; methodology, BR, ST, MM, AM, MJ, MK, PD.; software, MM, AM.; investigation, BR, HT, ST.; writing—original draft preparation, BR, AM, RA, KK.; writing—review and editing, BR, PD, RA, KK.; supervision, BR, KK; All authors have read and agreed to the published version of the manuscript.

Funding: KK laboratory is supported by grants from the National Health and Medical Research Council, Cancer Council Queensland, and National Breast Cancer Foundation.

Institutional Review Board Statement: All protocols were approved by the QIMR Berghofer Medical Research Institute Ethics and safety Committee valid to 2023 (Ethics number A0707-606M, Project numbers: 473, 674). All cell lines used in this study were obtained from ATCC as noted in the material and methods.

Acknowledgments: We acknowledge Dr. Prahlad Raninga, Dr. Devathri Nanayakkara and all members of the Signal transduction laboratory for their critical comments and advice. Dr. Andrea Rabellino for his contribution in editing some parts of this manuscript. In addition, we appreciate the critical review and comments of Prof. Jonathan Harris.

Conflicts of Interest: The authors declare no conflict of interest.

References

1. 1. Gouge, J.; Satia, K.; Guthertz, N.; Widya, M.; Thompson, A.J.; Cousin, P.; Dergai, O.; Hernandez, N.; Vannini, A. Redox signaling by the RNA polymerase III TFIIB-related factor Brf2. *Cell* **2015**, *163*, 1375–1387.
2. 2. Srihari, S.; Kalimutho, M.; Lal, S.; Singla, J.; Patel, D.; Simpson, P.T.; Khanna, K.K.; Ragan, M.A. Understanding the functional impact of copy number alterations in breast cancer using a network modeling approach. *Mol. Biosyst.* **2016**, *12*, 963–972.
3. 3. Ng, C.K.Y.; Martelotto, L.G.; Gauthier, A.; Wen, H.-C.; Piscuoglio, S.; Lim, R.S.; Cowell, C.F.; Wilkerson, P.M.; Wai, P.; Rodrigues, D.N.; et al. Intra-tumor genetic heterogeneity and alternative driver genetic alterations in breast cancers with heterogeneous HER2 gene amplification. *Genome Biol.* **2015**, *16*, 107, doi:10.1186/s13059-015-0657-6.
4. 4. Lockwood, W.W.; Chari, R.; Coe, B.P.; Thu, K.L.; Garnis, C.; Malloff, C.A.; Campbell, J.; Williams, A.C.; Hwang, D.; Zhu, C.-Q. Integrative genomic analyses identify BRF2 as a novel lineage-specific oncogene in lung squamous cell carcinoma. *PLoS Med* **2010**, *7*, e1000315.
5. 5. Garcia, M.J.; Pole, J.C.M.; Chin, S.-F.; Teschendorff, A.; Naderi, A.; Ozdag, H.; Vias, M.; Kranjac, T.; Subkhankulova, T.; Paish, C. A 1 Mb minimal amplicon at 8p11–12 in breast cancer identifies new candidate oncogenes. *Oncogene* **2005**, *24*, 5235–5245.
6. 6. Lu, M.; Tian, H.; Yue, W.; Li, L.; Li, S.; Qi, L.; Hu, W.; Gao, C.; Si, L. Overexpression of TFIIB-related factor 2 is significantly correlated with tumor angiogenesis and poor survival in patients with esophageal squamous cell cancer. *Med. Oncol.* **2013**, *30*, 553.
7. 7. Tian, Y.; Lu, M.; Yue, W.; Li, L.; Li, S.; Gao, C.; Si, L.; Qi, L.; Hu, W.; Tian, H. TFIIB-related factor 2 is associated with poor prognosis of nonsmall cell lung cancer patients through promoting tumor epithelial-mesenchymal transition. *Biomed Res. Int.* **2014**, *2014*.
8. 8. Cabarcas, S.; Schramm, L. RNA polymerase III transcription in cancer: the BRF2 connection. *Mol. Cancer* **2011**, *10*, 47.
9. 9. Felton-Edkins, Z.A.; Kenneth, N.S.; Brown, T.R.P.; Daly, N.L.; Gomez-Roman, N.; Grandori, C.; Eisenman, R.N.; White, R.J. Direct regulation of RNA polymerase III transcription by RB, p53 and c-Myc. *Cell Cycle* **2003**, *2*, 180–183.
10. 10. Felton-Edkins, Z.A.; White, R.J. Multiple mechanisms contribute to the activation of RNA polymerase III transcription in cells transformed by papovaviruses. *J. Biol. Chem.* **2002**, *277*, 48182–48191.
11. 11. Willis, I.M. Rna polymerase iii. In *Ejb Reviews 1993*; Springer, 1994; pp. 29–39.
12. 12. Schramm, L.; Hernandez, N. Recruitment of RNA polymerase III to its target promoters. *Genes Dev.* **2002**, *16*, 2593–2620.
13. 13. Birkbak, N.J.; Wang, Z.C.; Kim, J.-Y.; Eklund, A.C.; Li, Q.; Tian, R.; Bowman-Colin, C.; Li, Y.; Greene-Colozzi, A.; Iglehart, J.D. Telomeric allelic imbalance indicates defective DNA repair and sensitivity to DNA-damaging agents. *Cancer Discov.* **2012**, *2*, 366–375.
14. 14. Popova, T.; Manié, E.; Rieunier, G.; Caux-Moncoutier, V.; Tirapo, C.; Dubois, T.; Delattre, O.; Sigal-Zafrani, B.; Bollet, M.; Longy, M. Ploidy and large-scale genomic instability consistently identify basal-like breast carcinomas with BRCA1/2 inactivation. *Cancer Res.* **2012**, *72*, 5454–5462.

15. 15. Abkevich, V.; Timms, K.M.; Hennessy, B.T.; Potter, J.; Carey, M.S.; Meyer, L.A.; Smith-McCune, K.; Broaddus, R.; Lu, K.H.; Chen, J. Patterns of genomic loss of heterozygosity predict homologous recombination repair defects in epithelial ovarian cancer. *Br. J. Cancer* **2012**, *107*, 1776–1782.
16. 16. Marquard, A.M.; Eklund, A.C.; Joshi, T.; Krzystanek, M.; Favero, F.; Wang, Z.C.; Richardson, A.L.; Silver, D.P.; Szallasi, Z.; Birkbak, N.J. Pan-cancer analysis of genomic scar signatures associated with homologous recombination deficiency suggests novel indications for existing cancer drugs. *Biomark. Res.* **2015**, *3*, 1–10.
17. 17. Burrell, R.A.; McClelland, S.E.; Endesfelder, D.; Groth, P.; Weller, M.-C.; Shaikh, N.; Domingo, E.; Kanu, N.; Dewhurst, S.M.; Gronroos, E. Replication stress links structural and numerical cancer chromosomal instability. *Nature* **2013**, *494*, 492–496.
18. 18. Carter, S.L.; Cibulskis, K.; Helman, E.; McKenna, A.; Shen, H.; Zack, T.; Laird, P.W.; Onofrio, R.C.; Winckler, W.; Weir, B.A. Absolute quantification of somatic DNA alterations in human cancer. *Nat. Biotechnol.* **2012**, *30*, 413–421.
19. 19. Van Loo, P.; Nordgard, S.H.; Lingjærde, O.C.; Russnes, H.G.; Rye, I.H.; Sun, W.; Weigman, V.J.; Marynen, P.; Zetterberg, A.; Naume, B. Allele-specific copy number analysis of tumors. *Proc. Natl. Acad. Sci.* **2010**, *107*, 16910–16915.
20. 20. Shukla, A.; Nguyen, T.H.M.; Moka, S.B.; Ellis, J.J.; Grady, J.P.; Oey, H.; Cristino, A.S.; Khanna, K.K.; Kroese, D.P.; Krause, L. Chromosome arm aneuploidies shape tumour evolution and drug response. *Nat. Commun.* **2020**, *11*, 1–14.
21. 21. Thangavelu, P.U.; Lin, C.-Y.; Vaidyanathan, S.; Nguyen, T.H.M.; Dray, E.; Duijf, P.H.G. Overexpression of the E2F target gene CENPI promotes chromosome instability and predicts poor prognosis in estrogen receptor-positive breast cancer. *Oncotarget* **2017**, *8*, 62167.
22. 22. Carter, S.L.; Eklund, A.C.; Kohane, I.S.; Harris, L.N.; Szallasi, Z. A signature of chromosomal instability inferred from gene expression profiles predicts clinical outcome in multiple human cancers. *Nat. Genet.* **2006**, *38*, 1043–1048.
23. 23. Taylor, A.M.; Shih, J.; Ha, G.; Gao, G.F.; Zhang, X.; Berger, A.C.; Schumacher, S.E.; Wang, C.; Hu, H.; Liu, J. Genomic and functional approaches to understanding cancer aneuploidy. *Cancer Cell* **2018**, *33*, 676–689.
24. 24. Bailey, M.H.; Tokheim, C.; Porta-Pardo, E.; Sengupta, S.; Bertrand, D.; Weerasinghe, A.; Colaprico, A.; Wendl, M.C.; Kim, J.; Reardon, B. Comprehensive characterization of cancer driver genes and mutations. *Cell* **2018**, *173*, 371–385.
25. 25. Peng, G.; Lin, C.C.-J.; Mo, W.; Dai, H.; Park, Y.-Y.; Kim, S.M.; Peng, Y.; Mo, Q.; Siwko, S.; Hu, R. Genome-wide transcriptome profiling of homologous recombination DNA repair. *Nat. Commun.* **2014**, *5*, 1–11.
26. 26. Cortes-Ciriano, I.; Lee, S.; Park, W.-Y.; Kim, T.-M.; Park, P.J. A molecular portrait of microsatellite instability across multiple cancers. *Nat. Commun.* **2017**, *8*, 1–12.
27. 27. Cortés-Ciriano, I.; Lee, J.J.-K.; Xi, R.; Jain, D.; Jung, Y.L.; Yang, L.; Gordenin, D.; Klimczak, L.J.; Zhang, C.-Z.; Pellman, D.S. Comprehensive analysis of chromothripsis in 2,658 human cancers using whole-genome sequencing. *Nat. Genet.* **2020**, *52*, 331–341.
28. 28. Hoadley, K.A.; Yau, C.; Wolf, D.M.; Cherniack, A.D.; Tamborero, D.; Ng, S.; Leiserson, M.D.M.; Niu, B.; McLellan, M.D.; Uzunangelov, V. Multiplatform analysis of 12 cancer types reveals molecular classification within and across tissues of origin. *Cell* **2014**, *158*, 929–944.
29. 29. Masiero, M.; Simões, F.C.; Han, H.D.; Snell, C.; Peterkin, T.; Bridges, E.; Mangala, L.S.; Wu, S.Y.-Y.; Pradeep, S.; Li, D. A core human primary tumor angiogenesis signature identifies the endothelial orphan receptor ELTD1 as a key regulator of angiogenesis. *Cancer Cell* **2013**, *24*, 229–241.
30. 30. Winter, S.C.; Buffa, F.M.; Silva, P.; Miller, C.; Valentine, H.R.; Turley, H.; Shah, K.A.; Cox, G.J.; Corbridge, R.J.; Homer, J.J. Relation of a hypoxia metagene derived from head and neck cancer to prognosis of multiple cancers. *Cancer Res.* **2007**, *67*, 3441–3449.
31. 31. Eustace, A.; Mani, N.; Span, P.N.; Irlam, J.J.; Taylor, J.; Betts, G.N.J.; Denley, H.; Miller, C.J.; Homer, J.J.; Rojas, A.M. A 26-gene hypoxia signature predicts benefit from hypoxia-modifying therapy in laryngeal cancer but not bladder cancer. *Clin. cancer Res.* **2013**, *19*, 4879–4888.
32. 32. Sørensen, B.S.; Toustrup, K.; Horsman, M.R.; Overgaard, J.; Alsner, J. Identifying pH independent hypoxia induced genes in human squamous cell carcinomas in vitro. *Acta Oncol. (Madr).* **2010**, *49*, 895–905.
33. 33. Seigneuric, R.; Starmans, M.H.W.; Fung, G.; Krishnapuram, B.; Nuyten, D.S.A.; van Erk, A.; Magagnin, M.G.; Rouschop, K.M.; Krishnan, S.; Rao, R.B. Impact of supervised gene signatures of early hypoxia on patient survival. *Radiother. Oncol.* **2007**, *83*, 374–382.
34. 34. Ragnum, H.B.; Vlatkovic, L.; Lie, A.K.; Axcrona, K.; Julin, C.H.; Frikstad, K.M.; Hole, K.H.; Seierstad, T.; Lyng, H. The tumour hypoxia marker pimonidazole reflects a transcriptional programme associated with aggressive prostate cancer. *Br. J. Cancer* **2015**, *112*, 382–390.
35. 35. Hu, Z.; Fan, C.; Livasy, C.; He, X.; Oh, D.S.; Ewend, M.G.; Carey, L.A.; Subramanian, S.; West, R.; Ikpatt, F. A compact VEGF signature associated with distant metastases and poor outcomes. *BMC Med.* **2009**, *7*, 1–14.
36. 36. An, Y.; Bi, F.; You, Y.; Liu, X.; Yang, Q. Development of a novel autophagy-related prognostic signature for serous ovarian cancer. *J. cancer* **2018**, *9*, 4058.
37. 37. Malta, T.M.; Sokolov, A.; Gentles, A.J.; Burzykowski, T.; Poisson, L.; Weinstein, J.N.; Kamińska, B.; Huelsken, J.; Omberg, L.; Gevaert, O. Machine learning identifies stemness features associated with oncogenic dedifferentiation. *Cell* **2018**, *173*, 338–354.
38. 38. Hess, K.R.; Anderson, K.; Symmans, W.F.; Valero, V.; Ibrahim, N.; Mejia, J.A.; Booser, D.; Theriault, R.L.; Buzdar, A.U.; Dempsey, P.J. Pharmacogenomic predictor of sensitivity to preoperative chemotherapy with paclitaxel and fluorouracil, doxorubicin, and cyclophosphamide in breast cancer. *J. Clin. Oncol.* **2006**, *24*, 4236–4244.

39. 39. Wolf, D.M.; Lenburg, M.E.; Yau, C.; Boudreau, A.; van't Veer, L.J. Gene co-expression modules as clinically relevant hallmarks of breast cancer diversity. *PLoS One* **2014**, *9*, e88309.
40. 40. Li, B.; Severson, E.; Pignon, J.-C.; Zhao, H.; Li, T.; Novak, J.; Jiang, P.; Shen, H.; Aster, J.C.; Rodig, S. Comprehensive analyses of tumor immunity: implications for cancer immunotherapy. *Genome Biol.* **2016**, *17*, 1–16.
41. 41. Wishart, D.S.; Feunang, Y.D.; Guo, A.C.; Lo, E.J.; Marcu, A.; Grant, J.R.; Sajed, T.; Johnson, D.; Li, C.; Sayeeda, Z. DrugBank 5.0: a major update to the DrugBank database for 2018. *Nucleic Acids Res.* **2018**, *46*, D1074–D1082.
42. 42. Morris, G.M.; Huey, R. W. Lind strong, MF. Sanner, RK Belew, DS Goodsell, AJ Olson, Software News and Updates AutoDock4 and AutoDockTools4: Automated Docking with Selective Receptor Flexibility. *J. Comput. Chem* **2009**, *16*, 2785–2791.
43. 43. Österberg, F.; Morris, G.M.; Sanner, M.F.; Olson, A.J.; Goodsell, D.S. Automated docking to multiple target structures: incorporation of protein mobility and structural water heterogeneity in AutoDock. *Proteins Struct. Funct. Bioinforma.* **2002**, *46*, 34–40.
44. 44. Trott, O.; Olson, A.J. AutoDock Vina: improving the speed and accuracy of docking with a new scoring function, efficient optimization, and multithreading. *J. Comput. Chem.* **2010**, *31*, 455–461.
45. 45. Assadollahi, V.; Rashidieh, B.; Alasvand, M.; Abdolahi, A.; Lopez, J.A. Interaction and molecular dynamics simulation study of Osimertinib (AstraZeneca 9291) anticancer drug with the EGFR kinase domain in native protein and mutated L844V and C797S. *J. Cell. Biochem.* **2019**, *120*, doi:10.1002/jcb.28575.
46. 46. Rashidieh, B.; Valizadeh, M.; Assadollahi, V.; Ranjbar, M.M. Molecular dynamics simulation on the low sensitivity of mutants of NEDD-8 activating enzyme for MLN4924 inhibitor as a cancer drug. *Am. J. Cancer Res.* **2015**, *5*.
47. 47. Verma, S.; Grover, S.; Tyagi, C.; Goyal, S.; Jamal, S.; Singh, A.; Grover, A. Hydrophobic interactions are a key to MDM2 inhibition by polyphenols as revealed by molecular dynamics simulations and MM/PBSA free energy calculations. *PLoS One* **2016**, *11*, e0149014.
48. 48. Maisuradze, G.G.; Liwo, A.; Scheraga, H.A. Relation between free energy landscapes of proteins and dynamics. *J. Chem. Theory Comput.* **2010**, *6*, 583–595.
49. 49. McKinley, K.L.; Cheeseman, I.M. Large-scale analysis of CRISPR/Cas9 cell-cycle knockouts reveals the diversity of p53-dependent responses to cell-cycle defects. *Dev. Cell* **2017**, *40*, 405–420.
50. 50. Hart, T.; Tong, A.H.Y.; Chan, K.; Van Leeuwen, J.; Seetharaman, A.; Aregger, M.; Chandrashekhar, M.; Hustedt, N.; Seth, S.; Noonan, A. Evaluation and design of genome-wide CRISPR/SpCas9 knockout screens. *G3 Genes, Genomes, Genet.* **2017**, *7*, 2719–2727.
51. 51. Rummukainen, J.; Kytölä, S.; Karhu, R.; Farnebo, F.; Larsson, C.; Isola, J.J. Aberrations of chromosome 8 in 16 breast cancer cell lines by comparative genomic hybridization, fluorescence in situ hybridization, and spectral karyotyping. *Cancer Genet. Cytogenet.* **2001**, *126*, 1–7.
52. 52. Olgudóttir, E. Potential oncogenes within the 8p12-p11 amplicon. Identification and functional testing in breast cancer cell lines.
53. 53. Network, C.G.A. Comprehensive molecular portraits of human breast tumours. *Nature* **2012**, *490*, 61.
54. 54. Ma, H.; Wu, Y.; Dang, Y.; Choi, J.-G.; Zhang, J.; Wu, H. Pol III promoters to express small RNAs: delineation of transcription initiation. *Mol. Ther. Acids* **2014**, *3*, e161.
55. 55. Papaleo, E.; Mereghetti, P.; Fantucci, P.; Grandori, R.; De Gioia, L. Free-energy landscape, principal component analysis, and structural clustering to identify representative conformations from molecular dynamics simulations: the myoglobin case. *J. Mol. Graph. Model.* **2009**, *27*, 889–899.
56. 56. Chopra, N.; Wales, T.E.; Joseph, R.E.; Boyken, S.E.; Engen, J.R.; Jernigan, R.L.; Andreotti, A.H. Dynamic allostery mediated by a conserved tryptophan in the Tec family kinases. *PLoS Comput. Biol.* **2016**, *12*, e1004826.
57. 57. Lowe, M.N.; Plosker, G.L. Bexarotene. *Am. J. Clin. Dermatol.* **2000**, *1*, 245–250.
58. 58. Gniadecki, R.; Assaf, C.; Bagot, M.; Dummer, R.; Duvic, M.; Knobler, R.; Ranki, A.; Schwandt, P.; Whittaker, S. The optimal use of bexarotene in cutaneous T-cell lymphoma. *Br. J. Dermatol.* **2007**, *157*, 433–440.
59. 59. Yang, W.; Soares, J.; Greninger, P.; Edelman, E.J.; Lightfoot, H.; Forbes, S.; Bindal, N.; Beare, D.; Smith, J.A.; Thompson, I.R. Genomics of Drug Sensitivity in Cancer (GDSC): a resource for therapeutic biomarker discovery in cancer cells. *Nucleic Acids Res.* **2012**, *41*, D955–D961.
60. 60. Lambert, J.M.; Berkenblit, A. Antibody–drug conjugates for cancer treatment. *Annu. Rev. Med.* **2018**, *69*, 191–207.
61. 61. Wright, W.E.; Pereira-Smith, O.M.; Shay, J.W. Reversible cellular senescence: implications for immortalization of normal human diploid fibroblasts. *Mol. Cell. Biol.* **1989**, *9*, 3088–3092.
62. 62. Dobbelstein, M.; Moll, U. Targeting tumour-supportive cellular machineries in anticancer drug development. *Nat. Rev. Drug Discov.* **2014**, *13*, 179–96, doi:10.1038/nrd4201.
63. 63. Thomas, M.C.; Chiang, C.-M. The general transcription machinery and general cofactors. *Crit. Rev. Biochem. Mol. Biol.* **2006**, *41*, 105–178, doi:10.1080/10409230600648736.
64. 64. D., G.; A.G., P. Transcription factor therapeutics: Long-shot or lodestone. *Curr. Med. Chem.* **2005**, *12*, 691–701.
65. 65. Drygin, D.; Lin, A.; Bliesath, J.; Ho, C.B.; O'Brien, S.E.; Proffitt, C.; Omori, M.; Haddach, M.; Schwaebe, M.K.; Siddiqui-Jain, A.; et al. Targeting RNA polymerase I with an oral small molecule CX-5461 inhibits ribosomal RNA synthesis and solid tumor growth. *Cancer Res.* **2011**, *71*, 1418–1430, doi:10.1158/0008-5472.CAN-10-1728.

66. 66. Quin, J.; Chan, K.T.; Devlin, J.R.; Cameron, D.P.; Diesch, J.; Cullinane, C.; Ahern, J.; Khot, A.; Hein, N.; George, A.J. Inhibition of RNA polymerase I transcription initiation by CX-5461 activates non-canonical ATM/ATR signaling. *Oncotarget* **2016**, *7*, 49800.
67. 67. Xu, H.; Di Antonio, M.; McKinney, S.; Mathew, V.; Ho, B.; O'Neil, N.J.; Dos Santos, N.; Silvester, J.; Wei, V.; Garcia, J. CX-5461 is a DNA G-quadruplex stabilizer with selective lethality in BRCA1/2 deficient tumours. *Nat. Commun.* **2017**, *8*, 1–18.
68. 68. Bruno, P.M.; Lu, M.; Dennis, K.A.; Inam, H.; Moore, C.J.; Sheehe, J.; Elledge, S.J.; Hemann, M.T.; Pritchard, J.R. The primary mechanism of cytotoxicity of the chemotherapeutic agent CX-5461 is topoisomerase II poisoning. *Proc. Natl. Acad. Sci.* **2020**, *117*, 4053–4060.
69. 69. Moir, R.D.; Willis, I.M. Regulation of pol III transcription by nutrient and stress signaling pathways. *Biochim. Biophys. Acta (BBA)-Gene Regul. Mech.* **2013**, *1829*, 361–375.
70. 70. Gjidoda, A.; Henry, R.W. RNA polymerase III repression by the retinoblastoma tumor suppressor protein. *Biochim. Biophys. Acta (BBA)-Gene Regul. Mech.* **2013**, *1829*, 385–392.
71. 71. Hirsch, H.A.; Jawdekar, G.W.; Lee, K.-A.; Gu, L.; Henry, R.W. Distinct mechanisms for repression of RNA polymerase III transcription by the retinoblastoma tumor suppressor protein. *Mol. Cell. Biol.* **2004**, *24*, 5989–5999.
72. 72. Guerra, B.; Issinger, O.-G. Protein kinase CK2 in human diseases. *Curr. Med. Chem.* **2008**, *15*, 1870–1886.
73. 73. Hockman, D.J.; Schultz, M.C. Casein kinase II is required for efficient transcription by RNA polymerase III. *Mol. Cell. Biol.* **1996**, *16*, 892–898.
74. 74. Ghavidel, A.; Schultz, M.C. TATA binding protein-associated CK2 transduces DNA damage signals to the RNA polymerase III transcriptional machinery. *Cell* **2001**, *106*, 575–584.
75. 75. Felton-Edkins, Z.A.; Fairley, J.A.; Graham, E.L.; Johnston, I.M.; White, R.J.; Scott, P.H. The mitogen-activated protein (MAP) kinase ERK induces tRNA synthesis by phosphorylating TFIIIB. *EMBO J.* **2003**, *22*, 2422–2432.
76. 76. Carracedo, A.; Pandolfi, P.P. The PTEN–PI3K pathway: of feedbacks and cross-talks. *Oncogene* **2008**, *27*, 5527–5541.
77. 77. Woiwode, A.; Johnson, S.A.S.; Zhong, S.; Zhang, C.; Roeder, R.G.; Teichmann, M.; Johnson, D.L. PTEN represses RNA polymerase III-dependent transcription by targeting the TFIIIB complex. *Mol. Cell. Biol.* **2008**, *28*, 4204–4214.
78. 78. Dasari, S.; Tchounwou, P.B. Cisplatin in cancer therapy: molecular mechanisms of action. *Eur. J. Pharmacol.* **2014**, *740*, 364–378.
79. 79. Basu, A.; Krishnamurthy, S. Cellular responses to Cisplatin-induced DNA damage. *J. Nucleic Acids* **2010**, *2010*.
80. 80. Sears, C.R.; Turchi, J.J. Complex cisplatin-double strand break (DSB) lesions directly impair cellular non-homologous end-joining (NHEJ) independent of downstream damage response (DDR) pathways. *J. Biol. Chem.* **2012**, *287*, 24263–24272.
81. 81. Martins, N.M.; Santos, Nag.; Curti, C.; Bianchi, M.; Santos, Ac. Cisplatin induces mitochondrial oxidative stress with resultant energetic metabolism impairment, membrane rigidification and apoptosis in rat liver. *J. Appl. Toxicol. An Int. J.* **2008**, *28*, 337–344.
82. 82. Gavande, N.S.; VanderVere-Carozza, P.S.; Hinshaw, H.D.; Jalal, S.I.; Sears, C.R.; Pawelczak, K.S.; Turchi, J.J. DNA repair targeted therapy: the past or future of cancer treatment? *Pharmacol. Ther.* **2016**, *160*, 65–83.
83. 83. Brozovic, A.; Ambriović-Ristov, A.; Osmak, M. The relationship between cisplatin-induced reactive oxygen species, glutathione, and BCL-2 and resistance to cisplatin. *Crit. Rev. Toxicol.* **2010**, *40*, 347–359.
84. 84. Ma, Q. Role of nrf2 in oxidative stress and toxicity. *Annu. Rev. Pharmacol. Toxicol.* **2013**, *53*, 401–426.
85. 85. Liu, S.; Hua, Y.; Wang, J.; Li, L.; Yuan, J.; Zhang, B.; Wang, Z.; Ji, J.; Kong, D. RNA polymerase III is required for the repair of DNA double-strand breaks by homologous recombination. *Cell* **2021**, *184*, 1314–1329.
86. 86. Li, Y.; Xing, Q.; Wei, Y.; Zhao, L.; Zhang, P.; Han, X.; Wang, J. Activation of RXR by bexarotene inhibits inflammatory conditions in human rheumatoid arthritis fibroblast-like synoviocytes. *Int. J. Mol. Med.* **2019**, *44*, 1963–1970.